LATTICE DYNAMICS

OF

LAYERED TRANSITION METAL DICHALCOGENIDES

by

William Gordon McMullan

B.Sc. Simon Fraser University 1981

THESIS SUBMITTED IN PARTIAL FULFILLMENT OF

THE REQUIREMENTS FOR THE DEGREE OF

MASTER OF SCIENCE

in the Department

of

Physics

SIMON FRASER UNIVERSITY

February 1983

APPROVAL

Name: William Gordon McMullan

Degree: Master of Science

Title of thesis: Lattice Dynamics of Layered Transition Metal Dichalcogenides

Examining Committee:

Chairperson: B. P. Clayman

J. C. Irwin
Senior Supervisor

M. Plischke

M.L.W. Thewalt

R. F. Frindt

Date Approved: February 18, 1983

PARTIAL COPYRIGHT LICENSE

I hereby grant to Simon Fraser University the right to lend my thesis, project or extended essay (the title of which is shown below) to users of the Simon Fraser University Library, and to make partial or single copies only for such users or in response to a request from the library of any other university, or other educational institution, on its own behalf or for one of its users. I further agree that permission for multiple copying of this work for scholarly purposes may be granted by me or the Dean of Graduate Studies. It is understood that copying or publication of this work for financial gain shall not be allowed without my written permission.

Title of Thesis/Project/Extended Essay

Lattice Dynamics of Layered Transition Metal Dichalcogenides

Author:

(signature)

William Gordon McMullan

(name)

Mar. 30/83

(date)

ABSTRACT

The lattice dynamics of the group Vb layered transition metal dichalcogenides have been studied by Raman scattering and the experimental results have been analyzed in terms of a valence force field model. Explicit expressions for the Brillouin zone centre phonon frequencies have been obtained from the model and have been used along with the experimentally measured Raman frequencies to evaluate the force parameters of the model for 2H-TaS_2 and 2H-NbS_2. This work represents the first complete analysis of the Raman spectrum of both the 2H and 3R polytypes of NbS_2.

An investigation of the Raman spectrum of Ag_xTaS_2 for various silver concentrations and as a function of temperature has also been undertaken. It has been found that for $x \lesssim 1/3$ and at temperatures below about 150-200K, three new "A" modes appear in the Raman spectrum with frequencies of 320, 335 and 427 cm^{-1}. The appearance of these modes has been attributed to zone-folding. Based on the force parameters evaluated for the valence force field model, the phonon dispersion curves of 2H-TaS_2 have been plotted and used to determine the origin of these zone-folded modes. The results indicate that the 427 cm^{-1} peak is due to zone-folding along the c^* axis while the 320 and 335 cm^{-1} peaks modes are believed to originate from either the K or M points of the Brillouin zone.

ACKNOWLEDGEMENTS

I would like to thank Dr. R. F. Frindt and Per Joensen for providing the sample crystals used in this work. I would also like to thank Gary Scott, for his help in extracting the eigenvalues of the dynamical matrix, and Ken Urquhart. Ken's knowledge of the S.F.U. computing system has certainly saved me a great deal of time.

I am grateful for the help and friendship provided by my co-workers, Gary Jackle, Robert Audas and, of course, Kamal Bardhan. Finally, I would very much like to thank Dr. J. C. Irwin for his advice and direction and for the enjoyable time I have spent working under his supervision.

I gratefully acknowledge the Natural Sciences and Engineering Research Council, and ultimately the tax-paying citizens of Canada, for their financial support.

TABLE OF CONTENTS

LIST OF TABLES

LIST OF FIGURES

I. Introduction

The layered transition metal dichalcogenides are so named because they consist of vertically stacked, very thin layers. Separating each layer is a gap referred to as the van der Waals gap in deference to the weak interlayer bonding forces. The strong intralayer bonding is covalent in nature and this contrast in bond strengths gives rise to the anistropy exhibited by many of the physical properties of these materials. A study of lattice dynamics can give quantitative information on the nature of the interatomic bonding and hence information on many of the physical properties of these compounds.

There are several experimental methods available for investigating the lattice dynamics of layered transition metal dichalcogenides, the most powerful of which is neutron scattering. Neutron scattering experiments have been carried out on relatively few transition metal dichalcogenides however, because of the difficulty in obtaining large crystals. Exceptions to this are $NbSe_2$, $TaSe_2$ and MoS_2 which have been examined by Wakabayashi et al. (1974, 1975) and Moncton et al. (1975, 1977). The most widely used methods for studying the lattice dynamics of the transition metal dichalcogenides have been optical techniques such as Raman scattering and far infrared spectroscopy (Karecki 1980, and references therein). Ultrasonic techniques have also been used (Skolnick et al. 1977, Jericho et al., 1980), but these experiments provide information only on the long wavelength acoustic phonon branches.

Valuable information on the bonding and physical properties of these materials (eg. specific heat, thermal conductivity, elastic constants) can be obtained by analyzing the results of these experiments in terms of

lattice dynamical models. A number of such models have been developed. The lattice dynamics of the semiconductors MoS_2 and PbI_2 have been described by a simple central force model (Bromley, 1971) and by valence force field models (Lucovsky 1977, Wakabayashi et al., 1975). More recently, Feldman (1982) has demonstrated that a valence force field model can be successfully used to interpret the lattice dynamics of the metallic compounds 2H-$TaSe_2$ and 2H-$NbSe_2$.

The work described in this thesis was initiated with a view to studying the lattice dynamics of the intercalated layered transition metal dichalcogenides. Such compounds are not only of fundamental interest but have many potential technical applications (Whittingham, 1978). In particular the bonding of the intercalate atoms and their effects on the physical properties of the host crystal are of great interest.

The first part of this work involves a Raman scattering investigation of the lattice dynamics of the group Vb layered transition metal dichalcogenides. Closed form expressions have been obtained for the zone centre phonons in terms of the force parameters of Feldman's model and these have been used to interpret the Raman spectra of 2H-$TaSe_2$, 2H-$NbSe_2$ and 2H-TaS_2 - compounds which have been the subject of a number previous optical investigations (Wang and Chen 1974, Holy et al. 1976, Holy 1977, Sugai et al., 1981).

This work also presents the first complete analysis of the Raman spectrum of both 2H and 3R-NbS_2. The only previously reported work involving the lattice dynamics of NbS_2 are incomplete Raman studies of both the 2H (Nakashima et al., 1982) and 3R polytypes (Nakashima et al. 1982, Onari et al., 1979). This relative paucity of information likely stems not from a lack of interest but from the difficulties involved in growing NbS_2 with a well defined structure. However Fisher and Sienko (1980) have

recently reported a technique for obtaining the desired polytype. In the course of their investigation they also found that the prevailing polytype was dependent on the concentration of Nb in $Nb_{1+x}S_2$ with the 2H polytype corresponding to $x \simeq 0$ and the 3R polytype to $x \gtrsim 0.07$. Stoichiometric 3R-NbS_2 was not observed. Later X-ray work (Powell and Jacobson, 1981) has shown that the excess Nb atoms reside in octahedral sites within the van der Waals gap.

In addition to the possible effects of the excess Nb atoms on the lattice dynamics of $Nb_{1+x}S_2$, this is also a system of interest from the point of view that NbS_2, unlike its sister compounds TaS_2, $TaSe_2$, and $NbSe_2$, does not undergo a charge density wave (CDW) transition (Wilson et al., 1975). The reason for this is apparently still unknown.

Finally, in the second part of this thesis, the Raman spectrum of silver intercalated TaS_2 (Ag_xTaS_2) is investigated. The intercalate atoms in Ag_xTaS_2 have been observed to undergo an order-disorder transition at temperatures below room temperature (Scholz et al., 1982a and 1982b). Additional Raman active modes have been observed from the ordered state in these compounds. The appearance of these modes has been interpreted in terms of the phonon dispersion curves predicted by the lattice dynamical model developed for pure (ie. unintercalated) TaS_2.

II. Theory

2.1 Crystal Structure

The group Vb transition metal dichalcogenides (hereafter referred to as MX_2 compounds) consist of three hexagonally packed sheets where a sheet of metal atoms (M = Ta or Nb) is sandwiched between two sheets of chalcogen atoms (X = S or Se) (Wilson and Yoffe, 1969). Each set of three sheets is referred to as a layer and the layers are stacked on top of one another separated by a gap of approximately the same width as the sandwich.

Different stacking arrangements of the layers and of the sheets within a layer give rise to different polytypes of a particular MX_2 compound. Each polytype is given a prefix, eg. 1T, 2H, 3R, where the number refers to the number of layers within a unit cell and the letter to the symmetry of the unit cell (trigonal, hexagonal, rhombohedral). In both the 2H and 3R polytypes the metal atom is situated at the centre of a trigonal prism formed by six chalcogen atoms. The crystal structure of the 2H polytype is illustrated in Fig. 2.1. The various bond lengths, bond angles and lattice parameters shown in the figure are listed in Table 2.1 for several MX_2 compounds.

Calculations involving the 2H-MX_2 compounds have been carried out using the lattice vectors (Fig. 2.1c)

$$\vec{a} = a\left(\sqrt{3}/2\ \hat{x} + 1/2\ \hat{y}\right)$$
$$\vec{b} = a\left(-\sqrt{3}/2\ \hat{x} + 1/2\ \hat{y}\right)$$
$$\vec{c} = c\,\hat{z}$$

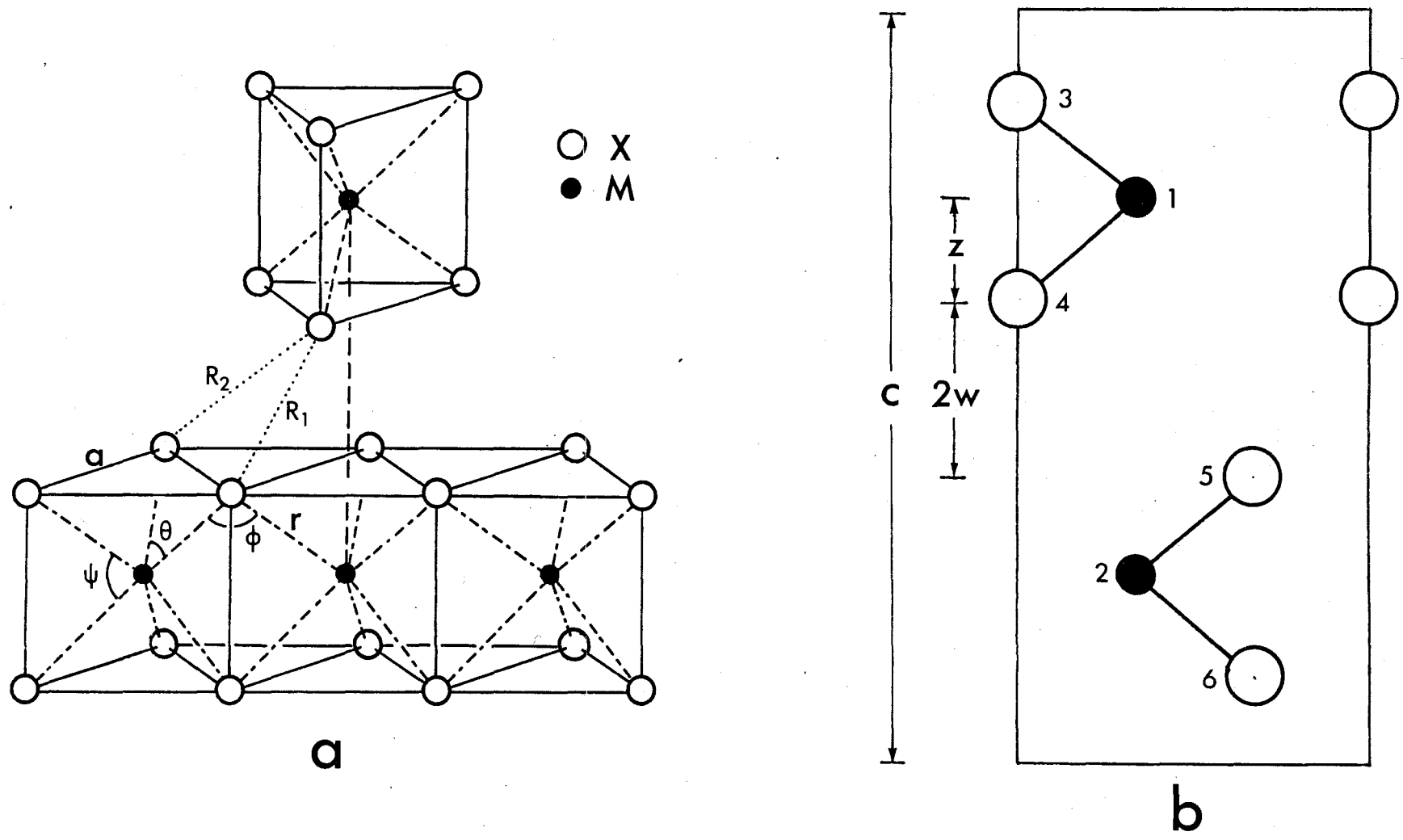

Figure 2.1 - Crystal Structure of 2H-MX_2 compounds. a) Bond lengths, bond angles and lattice parameters. b) 1120 section.

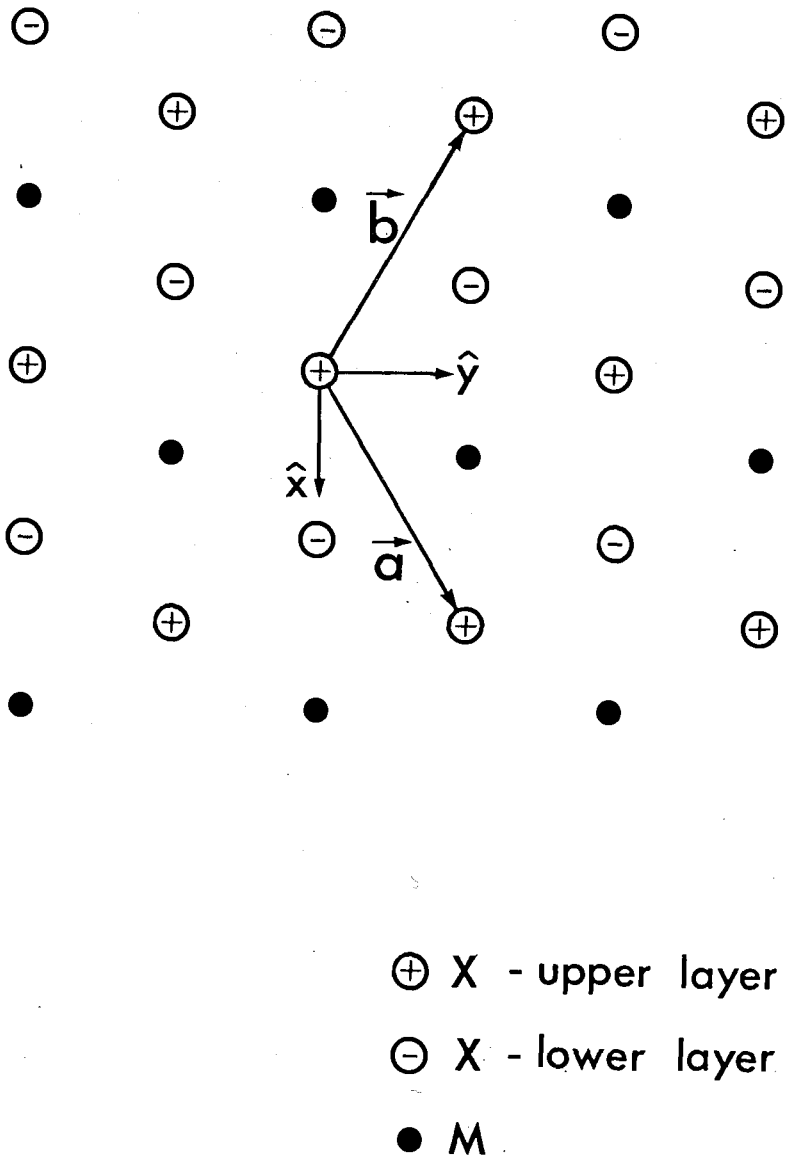

Figure 2.1c - In plane lattice vectors of the 2H-MX_2 compounds.

	$TaSe_2$	$NbSe_2$	TaS_2	NbS_2(2H)	NbS_2(3R)
a (A)	3.436[1]	3.45[1]	3.315[2]	3.31[1]	3.329[3]
c (A)	2x6.346[1]	2x6.282[1]	2x6.04[2]	2x5.95[1]	3x5.970[3]
r (A)	2.59[1]	2.60[1]	2.48*	2.47[1]	2.472[3]
z (A)	1.68[1]	1.68[1]	1.57[2]	1.57[1]	1.556*
w (A)	1.50[1]	1.46[1]	1.45*	1.40[1]	1.429*
R_1 (A)	3.59[1]	3.52[1]	3.48*	3.39[1]	3.444*
R_2 (A)	4.97*	4.93*	4.80*	4.74*	4.388*
ψ (deg)	80.2*	80.2*	78.72*	79.00[1]	78.00[3]
θ (deg)	83.1*	82.8[1]	83.9*	84.17[1]	84.53[3]
ϕ (deg)	83.1*	82.8*	83.9*	84.17*	84.53*

Table 2.1 - Structure parameters for group V layered transition metal dichalcogenides

References:
1 - Wilson and Yoffe, 1969
2 - Scholz and Frindt, 1980
3 - Powell and Jacobson, 1981
* - calculated from the parameters listed

The resulting reciprocal lattice vectors

$$\vec{a}^* = 4\pi/\sqrt{3}a\left(\tfrac{1}{2}\hat{x} + \sqrt{3}/2\,\hat{y}\right)$$
$$\vec{b}^* = 4\pi/\sqrt{3}a\left(-\tfrac{1}{2}\hat{x} + \sqrt{3}/2\,\hat{y}\right)$$
$$\vec{c}^* = \frac{2\pi}{c}\hat{z}$$

give rise to the Brillouin zone shown in Fig. 2.2. Several of the symmetry points in the zone have been labelled using the notational convention of Slater (1965).

The primitive cell of 3R-NbS_2 is rhombohedral and although the unit cell spans three layers it contains atoms from only one layer (Fig. 2.3b). The relationship between the rhombohedral and hexagonal axes are shown in Fig. 2.3a. The lattice parameters for 3R-NbS_2 are given in Table 2.1.

2.2 Group Theory

Group theory is a powerful tool in the analysis of the lattice dynamics of crystals. Armed with the knowledge of the crystal structure, the symmetry, degeneracy and optical activity of the normal modes of vibration can be determined from group theory (Burns 1977, Tinkham, 1964). The direction of the atomic vibrations for each normal mode can also be determined but the frequency of vibration requires specific knowledge of the interatomic forces involved.

The space group of the 2H-MX_2 compounds is D_{6h}^4 and it is non-symmorphic. The various group operations are given by Schluter (1979).

There are N=6 atoms per unit cell and hence 3N or 18 normal modes of vibration (for each wavevector) of which three are acoustic and 3N - 3 = 15 are optic. Infrared (IR) absorption and first order Raman scattering involves $\vec{q} = 0$ (or Γ point) phonons (see Fig 2.2 and Sec. 2.3) and thus

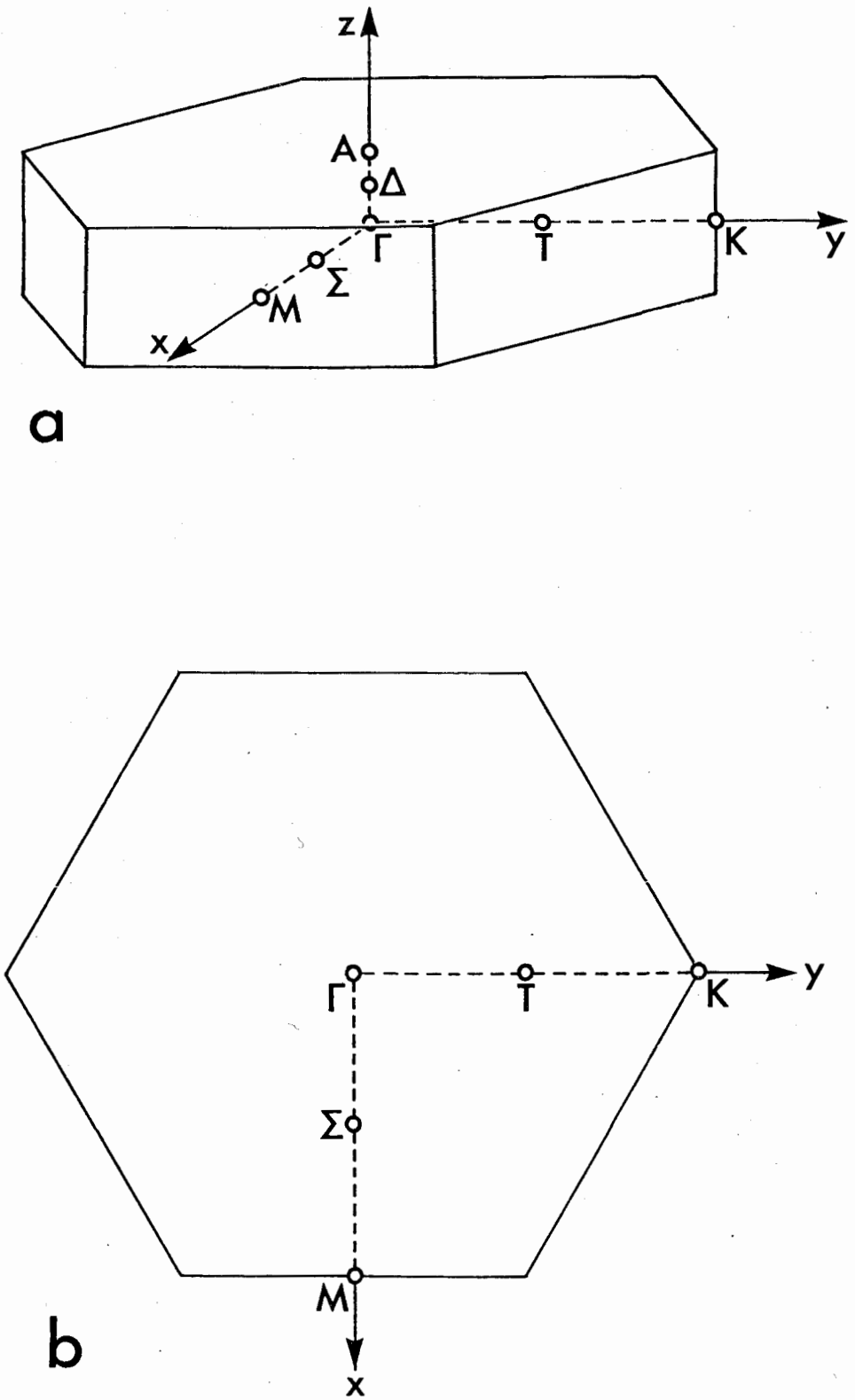

Figure 2.2 - Brillouin zone and symmetry points of 2H-MX_2 compounds.

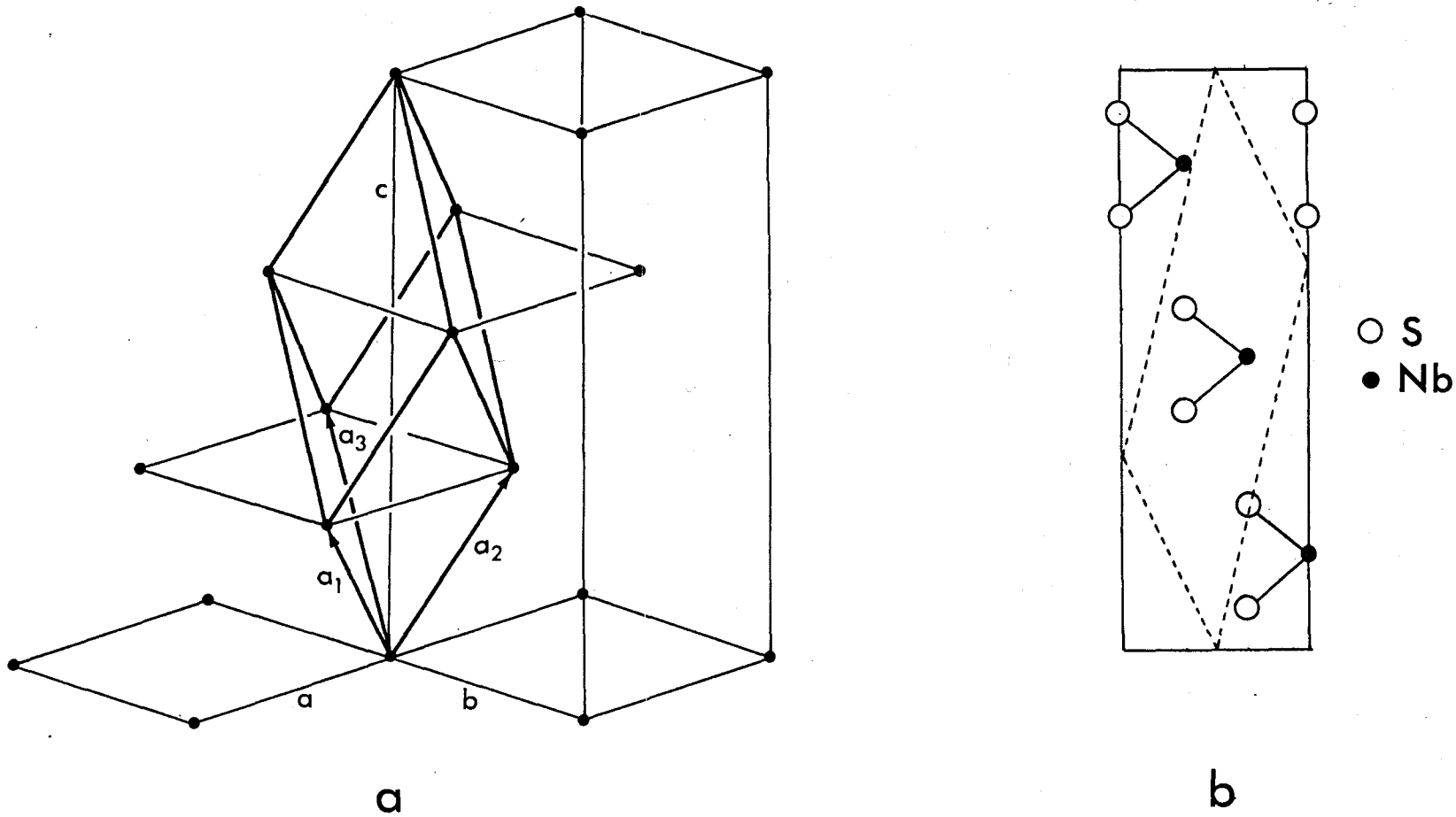

Figure 2.3 - Crystal structure of 3R-NbS_2. a) Relationship between trigonal (a_1,a_2,a_3) and hexagonal (a,b,c) lattice vectors. b) 1120 section of conventional unit cell with primitive unit cell shown by dashed lines.

attention is focussed on the modes at Γ.

The Γ point symmetry is that of the factor group of the crystal space group, in this case D_{6h}, and hence each Γ point phonon has the symmetry of an irreducible representation of D_{6h}. The reduction of the 18 normal modes into their irreducible representations can be carried out by a variety of methods. Perhaps the simplest is that given by Fateley et al. (1977) who describe the procedure in a step-by-step manner. Following this procedure for the 2H compounds leads to the reduction

$$\Gamma = A_{1g} \oplus 2B_{2g} \oplus E_{1g} \oplus 2E_{2g} \oplus 2A_{2u} \oplus B_{1u} \oplus 2E_{1u} \oplus E_{2u} \qquad (2.2.1)$$

The A and B modes involve vibrational motion perpendicular to the plane of the layers and are non-degenerate, while the doubly degenerate E representations designate modes with displacements in the layer. These modes have been calculated using the "transfer projection operator" method (Burns, 1977) and are shown schematically in Fig. 2.4.

A transition between vibrational states involves matrix elements of the form

$$\langle \psi^f_{vib} | Q | \psi^i_{vib} \rangle$$

where Q is the operator that induces the transition. In general $|\psi^i_{vib}\rangle$ is the ground state and group theoretical restrictions then permit transitions only when the irreducible representations of $|\psi^f_{vib}\rangle$ possess transformation properties that are compatible with Q. For Raman transitions, where Q is a second rank cartesian tensor (polarizability), the normal modes of vibration (ie. $|\psi^f_{vib}\rangle$) must transform as one of the components of the polarizability tensor, ie. as x^2, y^2, yz etc. For IR transitions, where Q is the dipole operator $e\vec{r}$, the normal modes must transform as x, y, or z.

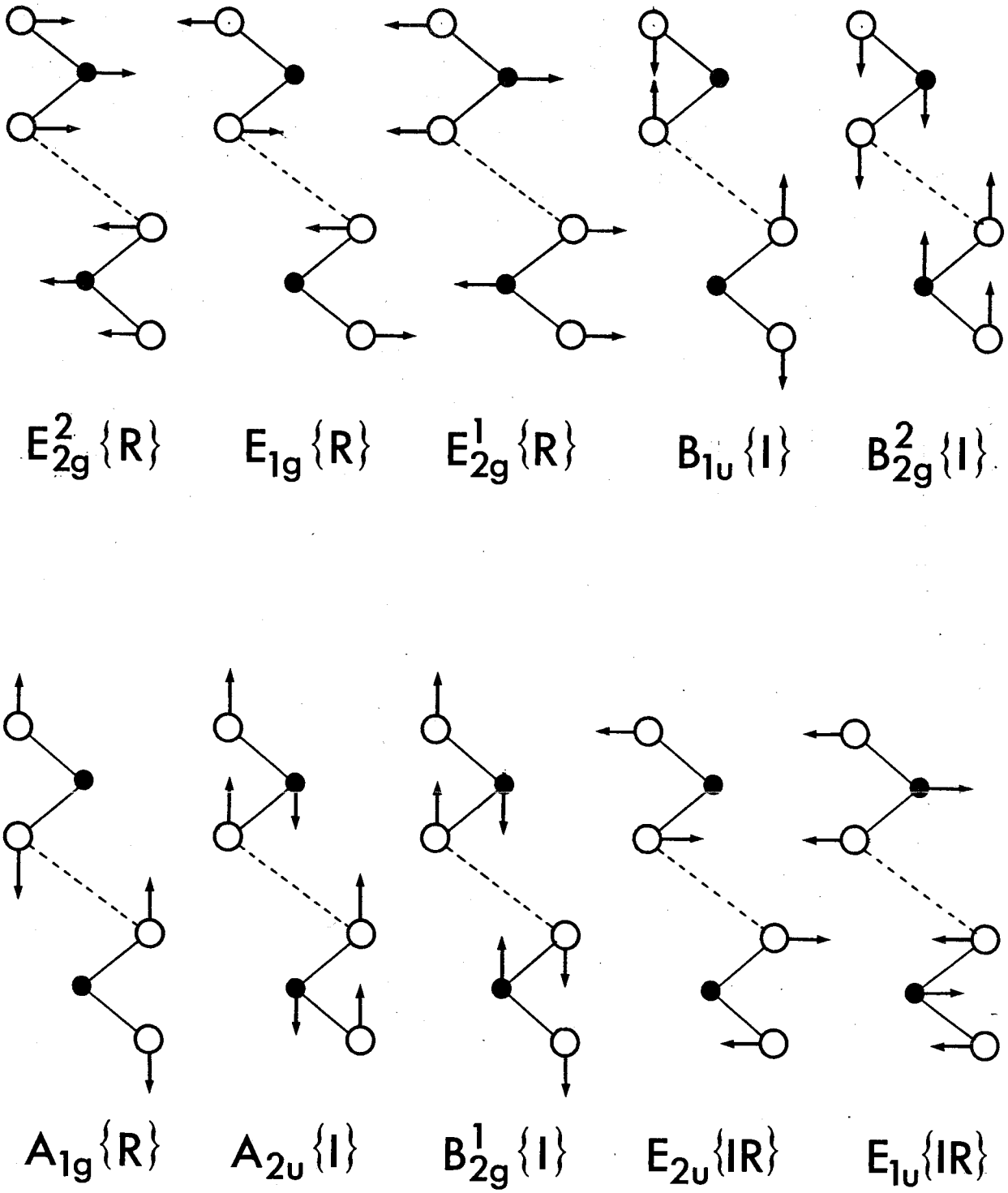

Figure 2.4 - Normal modes of the 2H-MX_2 compounds. The optical activity is indicated in brackets: R - Raman, IR - Infrared, I - inactive.

Acoustic modes have the same transformation properties as the IR active modes. A more detailed explanation of these transformation properties can be found in Burns (1977) or Heine (1960).

The transformation properties of the irreducible representations of all 32 crystallographic point groups are listed in the character tables of most books on group theory (eg. Burns, Tinkham) and hence the acoustic, IR and Raman active modes can be identified by inspection. From (2.2.1) and from the D_{6h} character tables (Fig. 2.5) the three acoustic modes are

$$A_{2u} \oplus E_{1u}$$

The remaining $A_{2u} + E_{1u}$ modes are IR active and there are four Raman active modes:

$$A_{1g} \oplus E_{1g} \oplus 2E_{2g}$$

The 3R-MX_2 compounds are characterized by the space group C_{3v}^5 (R3m). The Γ point symmetry is thus C_{3v} and the reduction of the nine zone centre normal modes into their irreducible representations is given by

$$3A_1 \oplus 3E$$

From the C_{3v} character tables (Fig. 2.5) it is seen that the three acoustic modes are $A_1 + E$ and that the remaining modes are simultaneously IR and Raman active. The atomic displacements for each of the modes can be found using correlation tables relating D_{6h} and C_{3v} point groups and from consideration of Fig. 2.4. These modes are shown in Fig. 2.6.

D_{6h}	E	$2C_6$	$2C_3$	C_2	$3C_2'$	$3C_2''$	i	$2S_3$	$2S_6$	$\sigma_h(xy)$	$3\sigma_d$	$3\sigma_v$		
A_{1g}	1	1	1	1	1	1	1	1	1	1	1	1		x^2+y^2, z^2
A_{2g}	1	1	1	1	-1	-1	1	1	1	1	-1	-1	R_z	
B_{1g}	1	-1	1	-1	1	-1	1	-1	1	-1	1	-1		
B_{2g}	1	-1	1	-1	-1	1	1	-1	1	-1	-1	1		
E_{1g}	2	1	-1	-2	0	0	2	1	-1	-2	0	0	(R_x, R_y)	(xz, yz)
E_{2g}	2	-1	-1	2	0	0	2	-1	-1	2	0	0		(x^2-y^2, xy)
A_{1u}	1	1	1	1	1	1	-1	-1	-1	-1	-1	-1		
A_{2u}	1	1	1	1	-1	-1	-1	-1	-1	-1	1	1	z	
B_{1u}	1	-1	1	-1	1	-1	-1	1	-1	1	-1	1		
B_{2u}	1	-1	1	-1	-1	1	-1	1	-1	1	1	-1		
E_{1u}	2	1	-1	-2	0	0	-2	-1	1	2	0	0	(x, y)	
E_{2u}	2	-1	-1	2	0	0	-2	1	1	-2	0	0		

Figure 2.5a - Character Table for D_{6h} point group.

C_{3v}	E	$2C_3$	$3\sigma_v$		
A_1	1	1	1	z	x^2+y^2, z^2
A_2	1	1	-1	R_z	
E	2	-1	0	(x, y) (R_x, R_y)	(x^2-y^2, xy) (xz, yz)

Figure 2.5b - Character Table for C_{3v} point group.

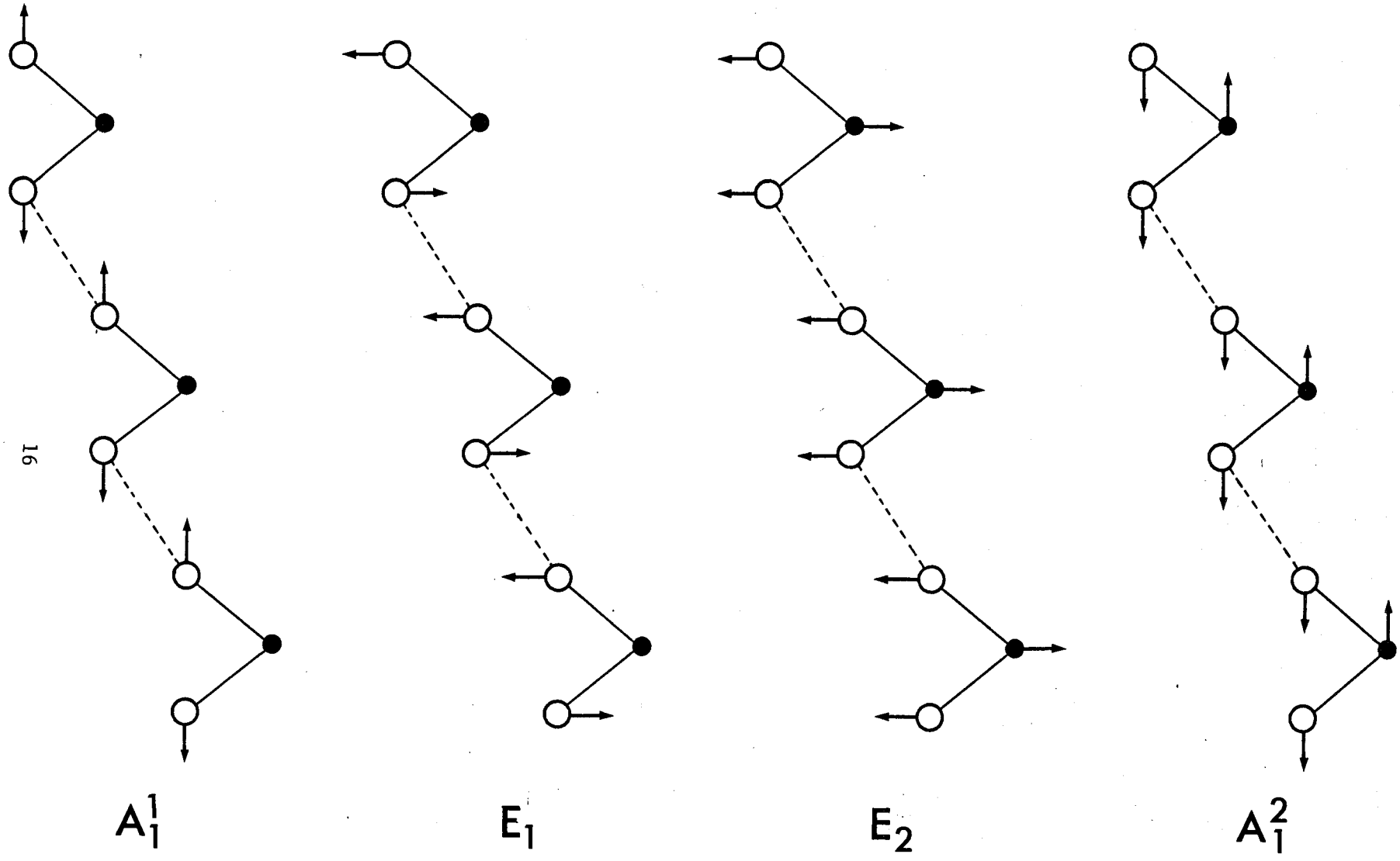

Figure 2.6 - Normal modes of 3R-NbS_2.

2.3 Raman Scattering

In this thesis Raman scattering refers to the inelastic scattering of light by phonons and can be treated with a classical, semi-classical or full quantum mechanical formalism.

Classically, when light impinges on a crystal it induces a dipole moment. The light scattered by the crystal can be considered to be radiation from the induced dipole moment μ , where μ is given by

$$\mu = \alpha E \tag{2.3.1}$$

and where $E = E_o \cos\omega_o t$ is the electric field associated with the incident radiation and α is the polarizability of the crystal. The lattice vibrations of the crystal will modulate the polarizability and if one expands α in terms of the atomic displacements u_j

$$\alpha = \alpha_o + \frac{\partial\alpha}{\partial u_j} u_j + \frac{\partial^2\alpha}{\partial u_i \partial u_j} u_i u_j + \cdots$$

$$\simeq \alpha_o + \alpha_1 \cos\omega_j t \tag{2.3.2}$$

the expression for the dipole moment becomes

$$\mu = \alpha_o E_o \cos\omega_o t + \alpha_1 E_o\left[\cos(\omega_o+\omega_j)t + \cos(\omega_o-\omega_j)t\right] \tag{2.3.3}$$

The intensity of the scattered radiation is proportional to $|\mu|^2$. The first term in (2.3.3) thus corresponds to scattered light unshifted in frequency (Rayleigh scattering) while the second and third terms correspond to inelastically scattered light shifted to higher

(Anti-stokes) and lower (Stokes) frequencies respectively. These latter two terms account for Raman scattering in the classical picture.

The modern approach to the analysis of Raman scattering utilizes quantum mechanics. Such a treatment is given by Loudon (1963, 1964, 1973) and an overview of some the relevant material is presented below.

From the quantum mechanical viewpoint, a Stokes (Anti-stokes) Raman scattering process involves the destruction of an incident photon of frequency ω_i, the creation (destruction) of a phonon of frequency ω and the creation of a scattered photon of lower (higher) frequency ω_s. Conservation of energy and momentum for the Stokes event can be written

$$\omega_i = \omega + \omega_s \tag{2.3.4}$$

$$\vec{k}_i = \vec{q} + \vec{k}_s \tag{2.3.5}$$

For photons in the visible range, $\omega_i \gg \omega$ and thus $\omega_i \approx \omega_s$. This in turn implies $|\vec{k}_i| \approx |\vec{k}_s|$ and hence from (2.3.5) $0 < |\vec{q}| \leq 2|\vec{k}_i|$. Since the size of the Brillouin zone is typically $\pi/a \sim 10^8 cm^{-1}$ and $|\vec{k}_i| \sim 10^5 cm^{-1}$, it is seen that only $\vec{q} \approx 0$ (long wavelength) phonons participate in first order Raman scattering.

The principle process governing Raman scattering is illustrated in Fig. 2.7b. The terms H_{er} and H_{el} represent the electron-radiation and electron-lattice interactions respectively. The electrons act only as an intermediary, coupling the radiation to the lattice. All electronic transitions are virtual and the initial and final electronic state is taken to be the ground state.

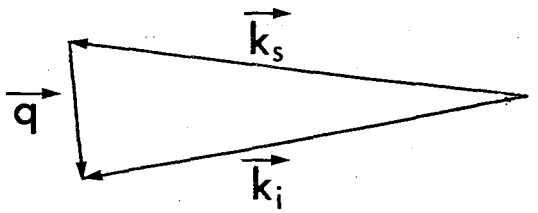

a

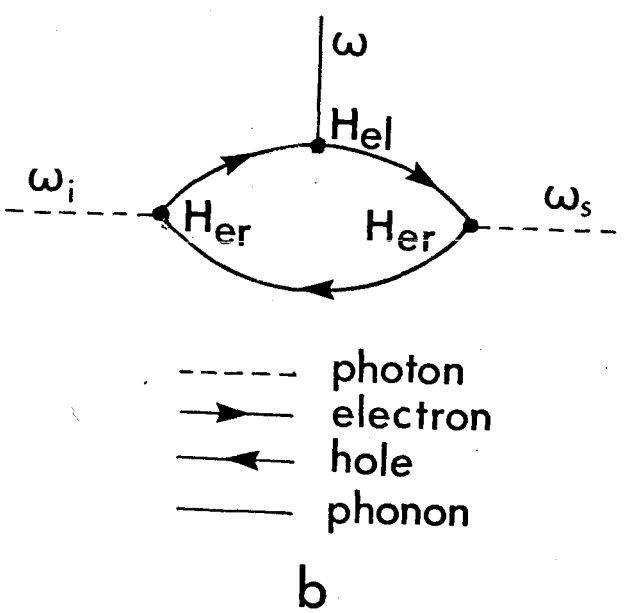

b

Figure 2.7 - Raman scattering. a) Scattering geometry (momentum conservation). b) Scattering process.

The probability per unit time of this process occurring is obtained from third order perturbation theory (Loudon, 1964):

$$W = \frac{2\pi}{\hbar^6} \sum_{\vec{q}\cdot\vec{k}_s} \left| \sum_{a,b} \frac{\langle n_i-1, 1, n_o+1, 0 | H_1 | a \rangle \langle a | H_1 | b \rangle \langle n_i, 0, n_o, 0 \rangle}{(\omega_a - \omega_i)(\omega_b - \omega_i)} \right|^2 \times$$

$$\times \delta(\omega_i - \omega - \omega_s) \qquad (2.3.6)$$

where n_i, 0, n_o indicates respectively the number of incident photons, scattered photons and optic phonons present in the initial state, and the final 0 indicates the electron is in its ground state. The sum is over all possible virtual intermediate states a and b and $H_1 = H_{el} + H_{er}$. The usual practice is to express H_{er} in terms of $\vec{A}\cdot\vec{p}$, where $\vec{A}$ is the vector potential and $\vec{p}$ the electron momentum, and to take H_{el} as the lattice deformation potential, ie. the perturbation, produced by the lattice vibrations, of the periodic potential acting on the electrons. Using these forms for H_{el} and H_{er} in (2.3.6) results in an expression for w propotional to $|R|^2$ where R is the Raman tensor and is defined in terms of the matrix elements appearing in (2.3.6).

In general R depends on the symmetry and frequency of the phonon, and the polarizations and frequencies of the incident and scattered photons. Physically however, R is essentially the same as the coefficient of the linear term in the Taylor series expansion of the polarizability tensor

$$\alpha_{\mu\nu} = \alpha^0_{\mu\nu} + \sum_{\sigma} \alpha'_{\mu\nu} u_\sigma + \sum_{\sigma,\tau} \alpha^2_{\mu\nu} u_\sigma u_\tau + \cdots \qquad (2.3.7a)$$

where $$\alpha'_{\mu\nu} \equiv \left.\frac{\partial \alpha_{\mu\nu}}{\partial u_\sigma}\right|_{u_\sigma=0} , \quad \alpha^2_{\mu\nu} \equiv \left.\frac{\partial^2 \alpha_{\mu\nu}}{\partial u_\sigma \partial u_\tau}\right|_{u_\sigma, u_\tau = 0} \qquad (2.3.7b)$$

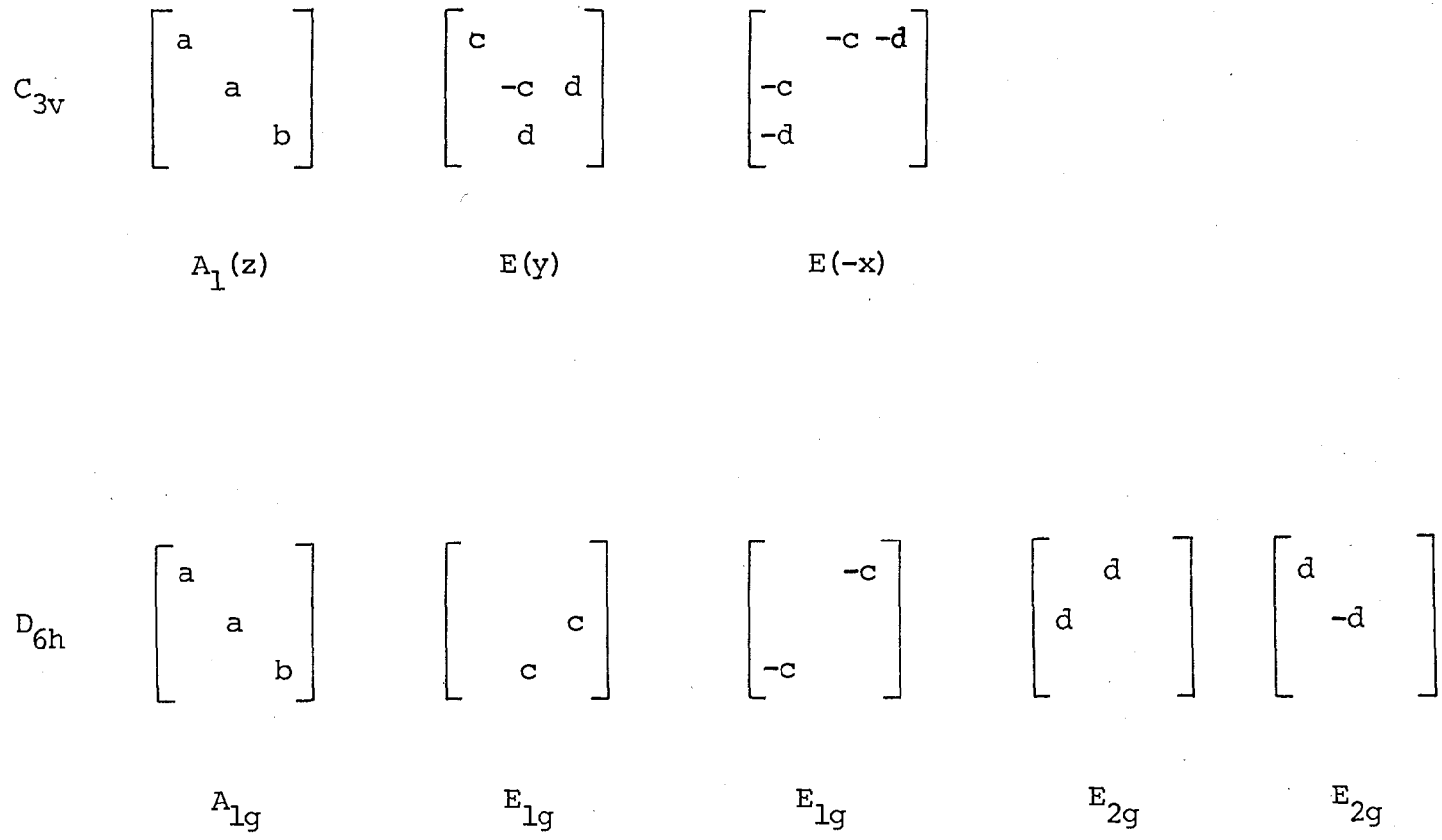

Figure 2.8 - Raman tensors for D_{6h} and C_{3v} point groups.

The utility of the Raman tensor arises form the fact that the scattering efficiency S, defined as the ratio of the number of incident photons to the number of scattered photons, is given by (Loudon, 1964)

$$S = A\left[\sum_{\substack{\mu,\nu \\ =x,y,z}} e^{i}_{\mu} R_{\mu\nu} e^{s}_{\nu}\right]^2 \qquad (2.3.8)$$

where A is a constant of proportionality and $\hat{e}^i$ ($\hat{e}^s$) is the direction of polarization of the incident (scattered) light. The form of R depends on the crystal symmetry and on the symmetry of the phonon. For a crystal of known symmetry and for Γ point phonons, the non-zero elements of R for each mode can be determined from group theory (Burns, 1977). Thus, as is evident from (2.3.8), by varying the incident and scattered polarizations experimentally, the symmetry of a particular phonon mode can be determined and compared to the symmetry predicted by group theory.

The Raman tensors for phonons with symmetries belonging to the D_{6h} and C_{3v} point groups are given in Fig. 2.8 (Loudon, 1964).

2.4 Second Order Raman Scattering

Second order Raman scattering is a two-phonon process involving either the creation or destruction of two phonons or the creation of one phonon and the destruction of another. The coefficient of the quadratic term in (2.3.7) gives rise to second order Raman scattering.

The conservation of energy and momentum conditions for the second order Stokes process are

$$\omega_i = \omega_q + \omega_{q'} + \omega_s$$

$$\vec{k}_i = \vec{q} + \vec{q}' + \vec{k}_s$$

and the restriction on the phonon wavevectors is

$$0 < |\vec{q} + \vec{q}'| \leq 2|\vec{k}_i| \qquad (2.4.1)$$

From (2.4.1) it is clear that the phonons participating in second order scattering must have essentially equal and opposite wavevectors but, in contrast to the first order process, scattering can be observed from all parts of the Brillouin zone. Hence, the second order Raman spectrum is proportional to the two-phonon denstiy of states - the intensity of a second order feature at frequency ω is dependent on the combined density of states of pairs of phonons whose frequency difference or sum is ω. The second order spectrum thus generally consists of a broad continuum background with superimposed peaks and shoulders that arise from singularities in the density of states.

2.5 Temperature Dependence of Raman Spectra

The intensity of peaks in first(second) order scattering is governed by the mean number of phonons in the appropriate state(s). This is given by the temperature dependent Bose-Einstein population factor

$$n = \left[\exp(\hbar\omega/kT) - 1 \right]^{-1}$$

This dependence on n is summarized in Table 2.2 (after Burstein, 1964).

Process		Stokes	Antistokes
1st Order	ω	$1 + n_j$	n_j
2nd Order (overtone)	2ω	$(1 + n_j)^2$	n_j^2
2nd Order (sum)	$\omega + \omega'$	$(1+n_j)(1+n_{j'})$	$n_j n_{j'}$
2nd Order (difference)	$\omega - \omega'$	$n_j n_{j'} + n_j$	$n_j n_{j'} + n_j$

Table 2.2 - Temperature dependence factors for Raman spectra.

2.6 Zone-folding

Later work in this thesis involving silver intercalated TaS_2 introduces the concept of zone-folding. This concept is breifly described here.

The presence of ordered intercalate ions introduces a new periodicity to the lattice that is described by new and larger lattice vectors. This new lattice is referred to as a 'superlattice'. Figure 2.9, for example, shows the lattice vectors that describe $\sqrt{3}a_o$ and $2a_o$ superlattices.

The larger superlattice unit cell results in a smaller Brillouin zone and hence points which were formerly situated away from the zone centre now occur at the centre of the new zone. These points are said to have been 'zone-folded' and being situated at the centre of the new zone may become Raman active.

Which points become zone-folded is dependent on the type of superlattice formed. In the case of a $2a_o$ superlattice, the M point is folded (Fig. 2.10a) and for a $\sqrt{3}a_o$ superlattice the K point is folded (Fig. 2.10b).

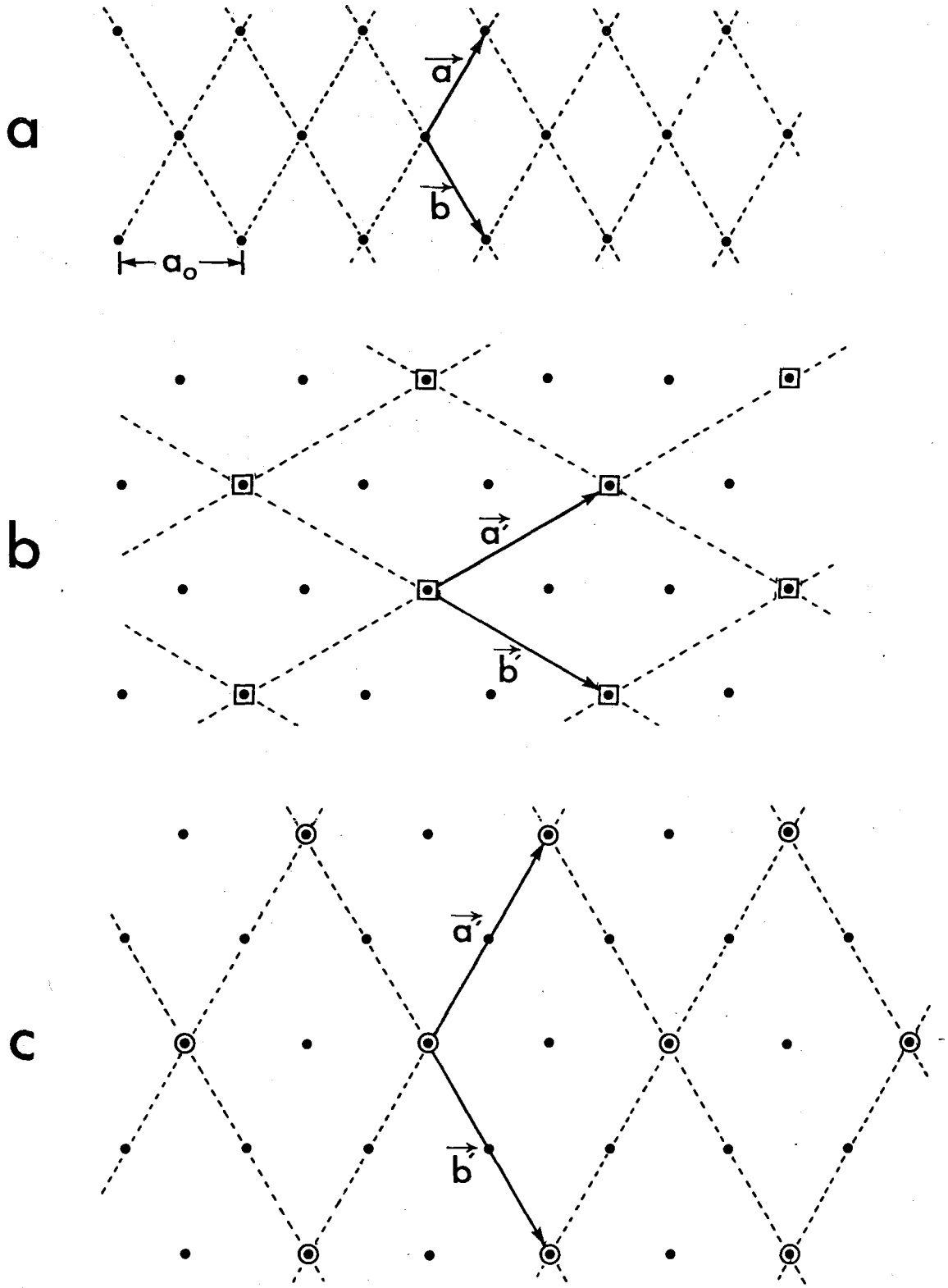

Figure 2.9 - Hexagonal superlattices. a) Undistorted lattice. b) $\sqrt{3}a_o$ superlattice, indicated by open squares. c) $2a_o$ superlattice indicated by open circles. Original lattice points are indicated by solid circles and the new lattice vectors are indicated by primes in b) and c).

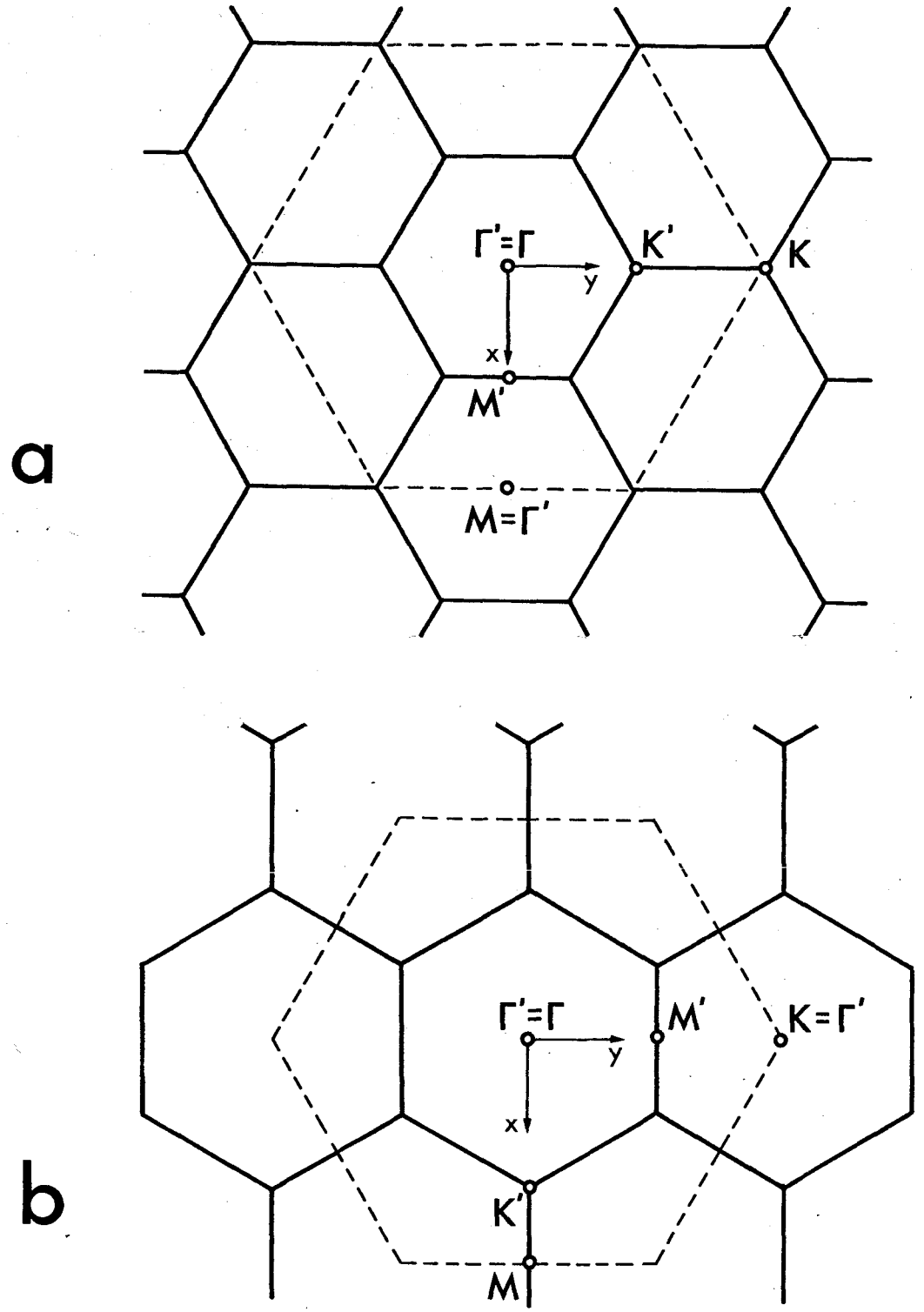

Figure 2.10 - Brillouin zone corresponding to a) a $2a_o$ superlattice and b) a $\sqrt{3}a_o$ superlattice. Symmetry points of the original zone (dashed lines) are unprimed, the new symmetry points are shown with primes.

III. Valence Force Field Model

3.1 Introduction

A number of lattice dynamical models have beem developed to account for experimentally observed Raman and IR spectra, neutron dispersion curves and velocity of sound data in the layered transition metal dichalcogenides. Probably the most frequently quoted model is that of Bromley (1971) which was originally developed for MoS_2 but which has been applied to many of the other layered materials (Agnihorti et al. 1973, Wang and Chen 1974, Holy 1977, Onari et al., 1979).

Bromley's model is very simple in that it incorporates only three intralayer central force constants and ideal geometry is assumed. Only a single layer is considered and hence the E^2_{2g} rigid layer mode (see Fig. 2.4) is not predicted. Bromley succeeded in obtaining closed form expressions for the phonon frequencies at the Γ, K, and M points of the Brillouin zone. This model predates all Raman scattering work on the group Vb MX_2 compounds and the expressions for the phonon frequencies at Γ have been widely used.

Bromley's model was subsequently modified to incorporate interlayer coupling. Expressions were introduced that included interlayer nearest neighbour shearing (Verble et al. 1972, Wieting 1973) and compressional (Wieting 1973) force constants whose values could be determined from measurements of the so called rigid layer modes.

Although Bromley's central force model is qualitatively correct for zone centre modes, it predicts more phonon dispersion than that observed

experimentally from neutron scattering. The valence force field (VFF) model, which is a model that includes force constants arising from bond angle bending as well as bond stretching, gives a better fit to the neutron data (Lucovsky 1977, Wakabayashi et al. 1975). Feldman (1982) has used a VFF model to fit Raman and neutron data for 2H-$TaSe_2$. The model successfully predicted one Raman mode not used in the fitting procedure and upon the appropriate mass changes all Raman and available neutron data for 2H-$NbSe_2$. The model involves four intralayer and two interlayer force constants as well as a phenomenological metal-metal interaction term introduced to account for the anomalous flattening of the Σ_1 acoustic branch observed by neutron diffraction (Moncton et al. 1977).

This model has been used to describe the work undertaken in this thesis and analytic closed form expressions have been obtained for all 18 zone centre phonon frequencies.

3.2 Lattice Dynamics

As a prelude to the lattice dynamical model to be introduced in the next section, a brief review of lattice dynamics is presented below. Further information on the subject can be obtained from most standard solid state physics texts (see for example Maradudin et al. 1963, Born and Huang 1954, Ashcroft and Mermin 1976).

The equilibrium position of atom κ in unit cell ℓ is given by

$$\vec{r}\begin{pmatrix}\ell\\ \kappa\end{pmatrix} = \vec{r}(\ell) + \vec{r}(\kappa) \qquad (3.2.1)$$

where $\vec{r}(\ell)$ is the position vector of unit cell ℓ and $\vec{r}(\kappa)$ is the equilibrium position of the atom within the cell. The potential energy Φ

of the crystal is assumed to be a function of the atomic positions and can be expanded in a Taylor series of the displacements $\vec{u}\binom{\ell}{\kappa}$ from equilibrium:

$$\Phi = \Phi_0 + \sum_{\mu} \sum_{\ell,\kappa} \Phi_\mu \binom{\ell}{\kappa} u_\mu \binom{\ell}{\kappa} + \\ + \frac{1}{2} \sum_{\mu,\nu} \sum_{\ell,\kappa} \sum_{\ell',\kappa'} \Phi_{\mu\nu} \binom{\ell\ \ell'}{\kappa\ \kappa'} u_\mu \binom{\ell}{\kappa} u_\nu \binom{\ell'}{\kappa'} + \cdots \quad (3.2.2)$$

where $$\Phi_\mu \binom{\ell}{\kappa} \equiv \left. \frac{\partial \Phi}{\partial u_\mu \binom{\ell}{\kappa}} \right|_0 \quad (3.2.3)$$

and $$\Phi_{\mu\nu} \binom{\ell\ \ell'}{\kappa\ \kappa'} \equiv \left. \frac{\partial^2 \Phi}{\partial u_\mu \binom{\ell}{\kappa} \partial u_\nu \binom{\ell'}{\kappa'}} \right|_0 \quad (3.2.4)$$

The subscript 0 in (3.2.3) and (3.2.4) indicates the term under consideration is to be evaluated at the equilibrium postion, and μ, ν are cartesian coordinates. The coefficient (3.2.3) of the linear term in (3.2.2) is seen to be the force acting on atom $\binom{\ell}{\kappa}$ at equilibrium and hence this term is zero. Terms of order u^3 and higher are neglected (harmonic approximation) which leads to the equations of motion

$$m_\kappa \ddot{u}_\mu \binom{\ell}{\kappa} = -\frac{1}{2} \sum_{\nu} \sum_{\ell',\kappa'} \Phi_{\mu\nu} \binom{\ell\ \ell'}{\kappa\ \kappa'} u_\nu \binom{\ell'}{\kappa'} \quad (3.2.5)$$

From (3.2.5) the physical interpretation of (3.2.4) is clear: it is the force in the μ direction on atom $\binom{\ell}{\kappa}$ due to a unit displacement in the ν direction of atom $\binom{\ell'}{\kappa'}$.

The solutions to (3.2.5) are assumed to be of plane wave form:

$$u_\mu \binom{\ell}{\kappa} = \frac{1}{\sqrt{m_\kappa}} u_\mu(\kappa) \exp i\left[\omega t - \vec{q} \cdot \vec{r}(\ell)\right] \quad (3.2.6)$$

Substitution of (3.2.6) into (3.2.5) and taking advantage of the

restrictions on (3.2.4) imposed by lattice periodicity (Maradudin et al., 1963) reduces the infinite set of equations (3.2.5) to a set of 3N coupled equations

$$\omega^2 u_\mu(\kappa) = \sum_{\nu,\kappa'} D_{\mu\nu}\left(\begin{smallmatrix}\vec{q}\\ \kappa\kappa'\end{smallmatrix}\right) u_\nu(\kappa') \qquad (3.2.7)$$

where

$$D_{\mu\nu}\left(\begin{smallmatrix}\vec{q}\\ \kappa\kappa'\end{smallmatrix}\right) = \sum_{\ell} \frac{1}{\sqrt{m_\kappa m_{\kappa'}}} \Phi_{\mu\nu}\left(\begin{smallmatrix}\ell\\ \kappa\kappa'\end{smallmatrix}\right) e^{-i(\vec{q}\cdot\vec{r}(\ell))} \qquad (3.2.8)$$

and $\ell \equiv \ell - \ell'$ is a consequence of the above mentioned restriction on (3.2.4). There will be solutions to (3.2.7) if and only if

$$\left| D_{\mu\nu}\left(\begin{smallmatrix}\vec{q}\\ \kappa\kappa'\end{smallmatrix}\right) - \omega^2 \delta_{\mu\nu}\delta_{\kappa\kappa'} \right| = 0 \qquad (3.2.9)$$

The 3Nx3N matrix $D_{\mu\nu}$ appearing in (3.2.9) is known as the dynamical matrix and its eigenvalues are the squares of the normal mode frequencies. These frequencies are dependent on $\vec{q}$.

3.3 VFF Model

The essence of the model used in this work is the assumption that the potential energy for the crystal can be written

$$\Phi = \tfrac{1}{2}\sum_{X\text{-}M} k_r(\Delta r)^2 + \tfrac{1}{2}\sum_{X\text{-}X} k_{R1}(\Delta R1)^2 + \tfrac{1}{2}\sum_{X\text{-}X} k_{R2}(\Delta R2)^2$$
$$+ \tfrac{1}{2}\sum_{X\text{-}M\text{-}X} k_\theta(r\Delta\theta)^2 + \tfrac{1}{2}\sum_{M\text{-}X\text{-}M} k_\phi(r\Delta\phi)^2 + \tfrac{1}{2}\sum_{X\text{-}M\text{-}X} k_\psi(r\Delta\psi)^2 \qquad (3.3.1)$$

where bond lengths and angles are as shown in Fig. 2.1a.

The procedure used to calculate the dynamical matrix involves expressing Δr and $r\Delta\theta$ in terms of cartesian coordinates, determining all combinations of atoms that must appear in the sums in (3.3.1), and then differentiating the terms in (3.3.1) to construct the matrices (3.2.4). These martrices are then summed according to (3.2.8) yielding the dynamical matrix. This procedure is outlined in more detail in Appendix I.

For the 2H compounds the dynamical matrix is an 18x18 complex Hermitian matrix and extracting the eigenvalues involves numerical methods and requires a computer. However, for the particular and important case of $\vec{q} = 0$, analytic expressions for the eigenvalues have been obtained by hand calculation. Identifying the correct frequency with the appropriate normal mode can be done by comparing the eigenvectors of the dynamical matrix to those calculated from group theory. The results are presented below:

$$\omega^2(A_{2u}) = 0 \tag{3.3.2a}$$

$$\omega^2(E_{1u}) = 0 \tag{3.3.2b}$$

$$\omega^2(E_{2u}) = \frac{1}{2m_x}\left(\frac{a}{r}\right)^2\left[k_r + (1-\cos\theta)^2 k_\theta + (1-\cos\phi)^2 k_\phi\right] \tag{3.3.2c}$$

$$\omega^2(E_{1g}) = \omega^2(E_{2u}) + \frac{a^2}{m_x}\left(\frac{1}{R1^2}k_{R1} + \frac{4}{R2^2}k_{R2}\right) \tag{3.3.2d}$$

$$\omega^2(B_{1u}) = \frac{3}{m_x}\left(\frac{z}{r}\right)^2\left[k_r + 2(1+\cos\psi)^2 k_\psi + 4(1-\cos\theta)^2 k_\theta + 4(1-\cos\phi)^2 k_\phi\right] \tag{3.3.2e}$$

$$\omega^2(A_{1g}) = \omega^2(B_{1u}) + \frac{24W^2}{m_x}\left(\frac{1}{R1^2}k_{R1} + \frac{1}{R2^2}k_{R2}\right) \quad (3.3.2f)$$

$$\omega^2(E_{1u}) = \frac{1}{2}\left(\frac{2m_x + m_M}{m_x m_M}\right)\left(\frac{a}{r}\right)^2\left[k_r + 2(1-\cos\psi)^2 k_\psi + (1-\cos\theta)^2 k_\theta + (1-\cos\phi)^2 k_\phi\right] \quad (3.3.2g)$$

$$\omega^2(A_{2u}) = 3\left(\frac{2m_x + m_M}{m_x m_M}\right)\left(\frac{z}{r}\right)^2\left[k_r + 4(1-\cos\theta)^2 k_\theta + 4(1-\cos\phi)^2 k_\phi\right] \quad (3.3.2h)$$

$$\omega^2(E^1_{2g}) = \frac{A + \sqrt{A^2-B}}{2} \quad (3.3.2i)$$

$$\omega^2(E^2_{2g}) = \frac{A - \sqrt{A^2-B}}{2} \quad (3.3.2j)$$

$$\omega^2(B^1_{2g}) = \frac{C + \sqrt{C^2-D}}{2} \quad (3.3.2k)$$

$$\omega^2(B^2_{2g}) = \frac{C - \sqrt{C^2-D}}{2} \quad (3.3.2l)$$

where

$$A = \omega^2(E_{1u}) + \omega^2(E_{1g}) - \omega^2(E_{2u})$$

$$B = \frac{8m_x}{2m_x + m_M}\,\omega^2(E_{1u})\left[\omega^2(E_{1g}) - \omega^2(E_{2u})\right]$$

$$C = \omega^2(A_{2u}) + \omega^2(A_{1g}) - \omega^2(B_{1u})$$

$$D = \frac{8m_x}{2m_x + m_M}\,\omega^2(A_{2u})\left[\omega^2(A_{1g}) - \omega^2(B_{1u})\right]$$

and m_M, m_X are the metal atom and chalcogen atom masses respectively, and where the lattice parameters, bond lengths and bond angles are as shown in Fig. 2.1.

IV. Experimental Procedure

4.1 Samples: Pure Crystals

The majority of the 3R-NbS_2 studied were provided by Dr. F. Levy of the Institut de Physique Appliquee in Lausanne, Switzerland, while all the 2H-MX_2 and the remainder of the 3R crystals were provided by Dr. R. F. Frindt and Per Joensen of the SFU Physics department. All crystals were grown using the iodine vapour transport technique.

The 3R-NbS_2, 2H-$TaSe_2$ and 2H-$NbSe_2$ crystals had smooth, mirror-like surfaces with a high metallic lustre. In contrast the 2H-TaS_2 and 2H-NbS_2 surfaces were a dull metallic blue-gray and badly wrinkled - reminiscent of crumpled tin foil. The sample dimensions were typically 5-10 mm^2 in area by 50-100μ thick.

The samples used for Raman studies were affixed to small copper disks using commercial nail polish.

After exposure to laser light for several hours the sample surfaces would occasionally deteriorate. In such cases a fresh surface could be exposed by cleaving the sample using 'Sell-o' brand adhesive tape.

Orientation of the 3R-NbS_2 sample was done by Laue X-ray back reflection. The Laue patterns for 2H-NbS_2 were not clear enough to determine the crystal axes and hence these crystals were oriented visually using hexagonal growth edges.

4.2 Samples: Intercalated Crystals

Several silver intercalated 2H-TaS_2 crystals were also examined by Raman scattering. These crystals were produced by cleaving pure TaS_2 crystals with 'Sell-o' tape. The cleaved sections were removed from the tape by dissolving the glue in trichloroethylene and the recovered crystals were then trimmed and placed in the intercalation cell shown in Fig. 4.1.

Silver ions from the $AgNO_3$ solution spontaneously intercalate between the layers of the TaS_2 crystal. The silver ions in solution are replenished from a piece of pure silver metal and overall electrical neutrality is maintained by pressing both the crystal and silver onto nickel foil with pieces of neoprene. This provides a path for electron flow between the silver metal and the crystal.

The intercalation process will continue until a saturation silver concentration of $x \simeq 2/3$ mole fraction is reached (Scholz and Frindt, 1980) but intermediate values of x can be obtained by removing the crystal before the reaction is complete. The silver concentration was determined by weighing the crystal before and after intercalation using a Cahn G-2 electrobalance.

Typical crystal dimensions were 1-2mm on a side by 2-10μ in thickness with a mass of 30-200 μgm. These smaller crystals were chosen to yield a more uniformly intercalated sample. Typical intercalation times are given in Table 4.1.

After intercalation the surfaces were observed to become rougher, more wrinkled, darker and less lustrous than the pure crystal. Homogeneity of the intercalated samples was inferred from (i) visual inspection, which indicated a basically uniform surface texture and colour; (ii) the Raman spectra of cleaved crystals, which did not change before and after

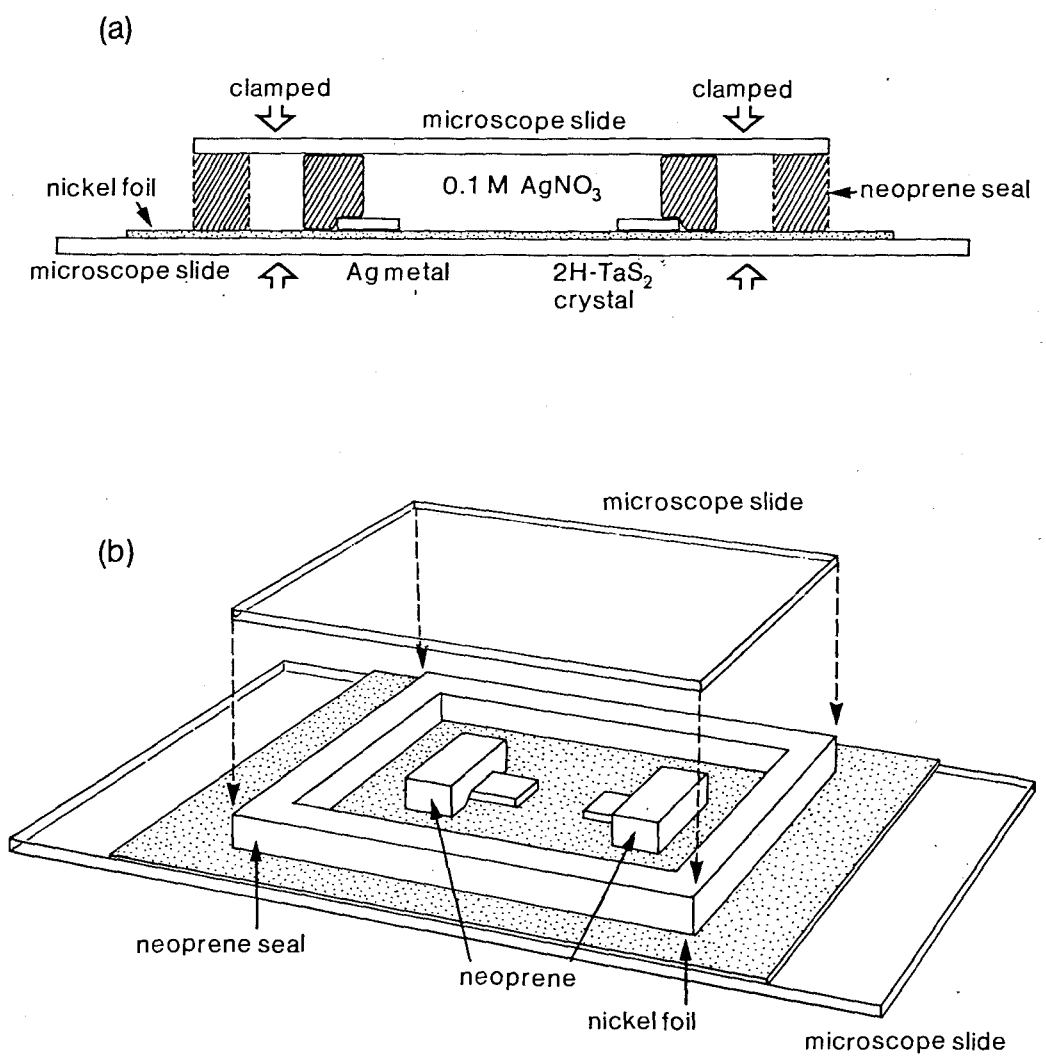

Figure 4.1 - Cell used to intercalate silver into 2H-TaS_2.

X	TIME (hrs.)
≤ 0.1	0.3 - 1.5
0.2	0.5 - 2
0.3	1 - 3
0.4	1 - 3.5
0.5	1.5 - 4
0.6	2 - 6

Table 4.1 - Typical intercalation times for Ag_xTaS_2

cleaving; and (iii) the fact that the Raman spectra obtained never indicated the presence of the unintercalated host crystal.

4.3 Raman Scattering Apparatus

Raman spectra were obtained using the system and backscattering geometry shown schematically in Fig. 4.2.

The sample was situated in an Air Products Displex model CSW-202 refrigeration system. The ambient crystal temperature could thus be controlled between the ranges 15-300K.

The incident light was provided by either a Spectra Physics model 165 or 170 argon ion laser tuned to 514.5 nm. The beam was circular in cross section but was focussed onto the sample in the shape of a thin line approximately 0.3 mm wide by 1 cm long by means of a cylindrical lens. This was done to reduce sample heating and to match the optics of the system. Output power from the laser was in the range 100-500mW but approximately 50% of this was lost before reaching the sample due to reflections at the various prisms used for beam alignment.

The scattered light was collected and focussed onto the entrance slit of a Spex 14018 double monochromator equipped with holographic gratings having 1800 rulings/mm. The slit widths that were typically used resulted in a bandpass of $3cm^{-1}$. The double monochromator was followed by a Spex 1442 single monochromator which provided a third diffraction grating.

The signal was detected by either an RCA C31034A-02 or ITT FW-130 photomultiplier tube. The tube was mounted in a Products for Research TE-104 refrigeration chamber and the dark count of the cooled tube was 5-10 counts/sec. The output from the tube was processed using standard photon

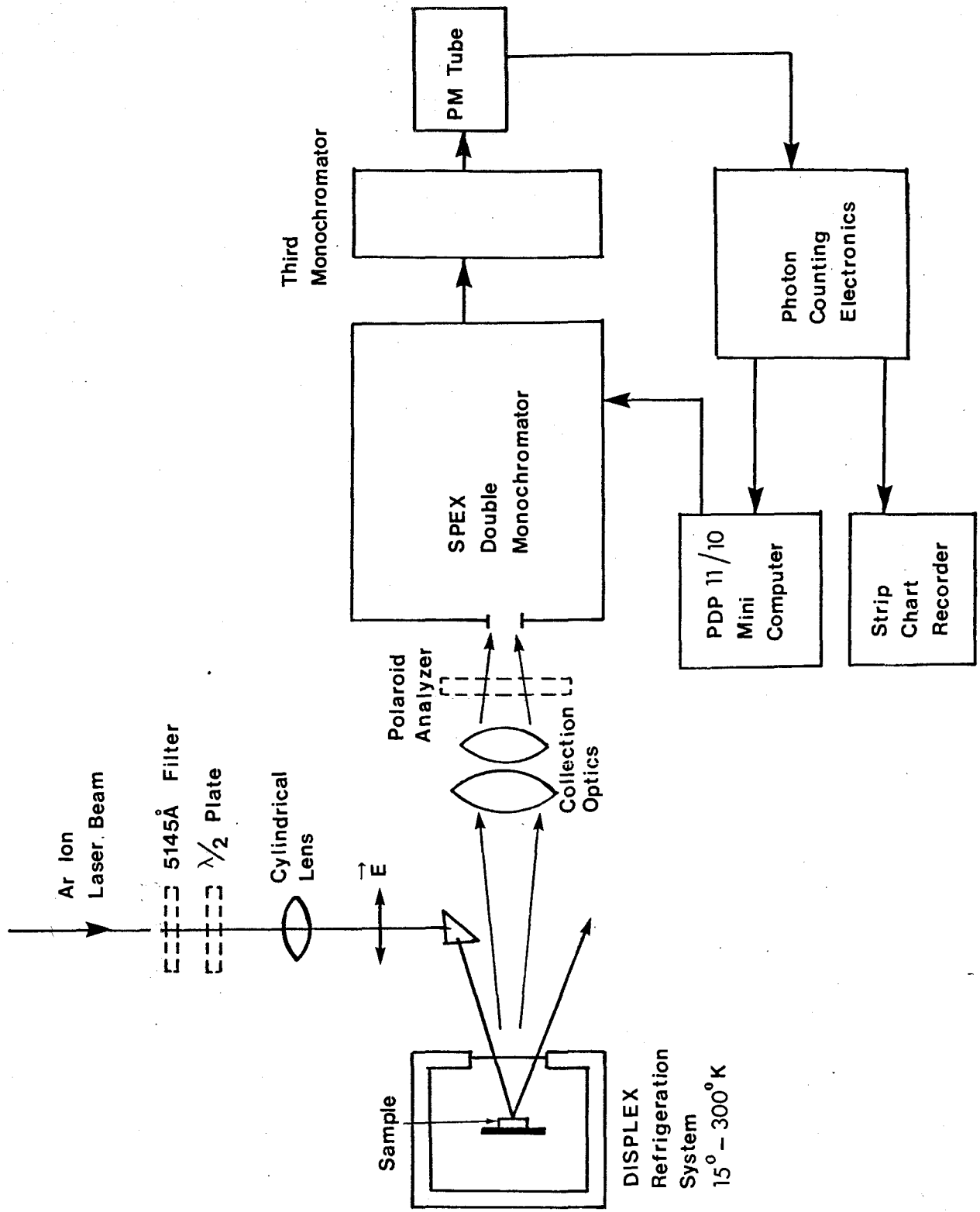

Figure 4.2 - Raman scattering apparatus in backscattering geometry.

counting electronics and the data displayed on a strip chart recorder and/or accumulated in a PDP11/10 mini-computer. The mini-computer was interfaced to the apparatus enabling the entire scanning operation to be done automatically if desired.

A 5145 A interference filter was generally used to eliminate unwanted argon plasma lines from the spectra. (The lines are sometimes desired for calibration purposes). The filter transmitted about 70% of the incident light.

To determine the polarization of the modes in NbS_2, a half-wave plate and polaroid analyzer were used as shown in Fig. 4.2. The direction of incident polarization could be set using the half-wave plate and scattered polarization selected using the analyzer. The notation used is such that, for example, 'XY' means the incident light is polarized in the x direction and the scattered light in the y direction, both with respect to the cartesian axes of the crystal.

In order to produce incident light polarized in the z direction, the 90° scattering configuration was used. This is shown in Fig. 4.3c. Because the angles θ and ϕ (Fig. 4.3) cannot be made zero for practical reasons, there is always some unwanted 'leakage' of the incident light into another direction. In Fig. 4.2a there is z leakage and x leakage in Fig. 4.2c.

The thinness of the crystals and fixed geometry of the apparatus prevented any analysis of scattered light polarized in the z direction.

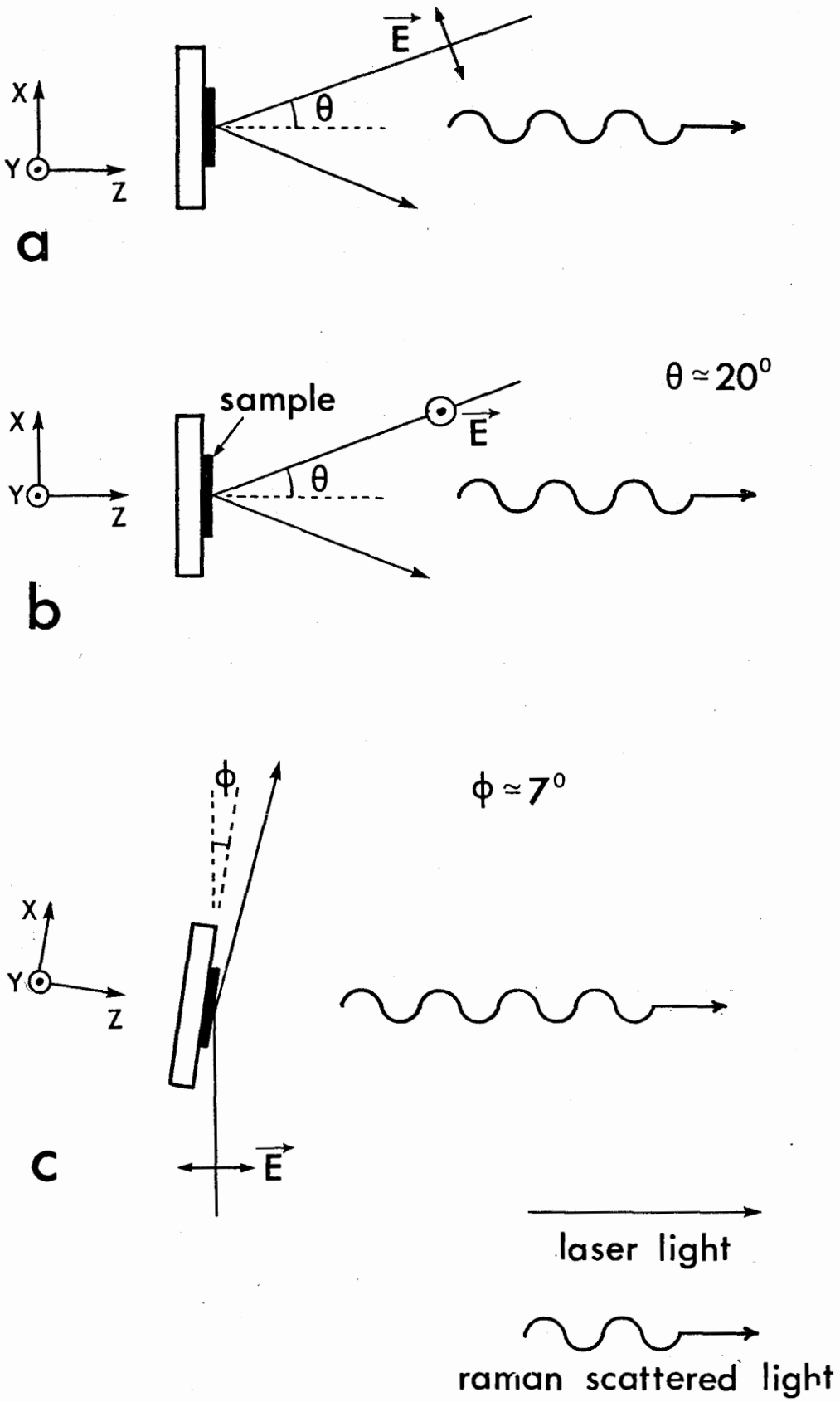

- Figure 4.3 - Scattering geometries that constitute a) $\hat{x}$ incident, b) $\hat{y}$ incident and c) $\hat{z}$ incident (90^{o} scattering).

V. Results and Discussion - Pure Crystals

5.1 Tantalum Diselenide and Niobium Diselenide

Room temperature Raman spectra of 2H-$TaSe_2$ and 2H-$NbSe_2$ are shown in Figs. 5.1 and 5.2. The results are similar to those previously reported (Wang and Chen 1974, Holy 1977) and the measured frequencies are displayed in Table 5.1.

The E_{1g} peak is too weak to be seen but the frequency has been determined by others and found to be 133 cm^{-1} in the case of $NbSe_2$ (Duffey et al. 1976) and 139 cm^{-1} for $TaSe_2$ (Holy 1977).

Both spectra are characterized by a broad feature occurring at about 150 cm^{-1} in $TaSe_2$ and about 180 cm^{-1} in $NbSe_2$. This feature is closely related to the charge density wave (CDW) that forms in these compounds. It arises from two-phonon scattering involving longitudinal acoustic (LA) phonons located in the vicinity of 2/3 ΓM (Klein 1982, Tsang et al., 1978). The LA phonon branch in these compounds exhibits a Kohn anomaly (Moncton et al. 1975, Wakabayashi et al. 1974) and consequently a higher two-phonon density of states. However, it has been shown (Maldague and Tsang, 1977) that the dominant contribution to the relatively large intensity of this mode is not the two-phonon density of states but rather is the strong electron-phonon coupling present in these compounds. This large electron-phonon coupling is closely associated with the presence of CDW's in these materials (Ibid.).

As the temperature is lowered and approaches the normal-ICDW (incommensurate charge density wave) transition temperature, this broad

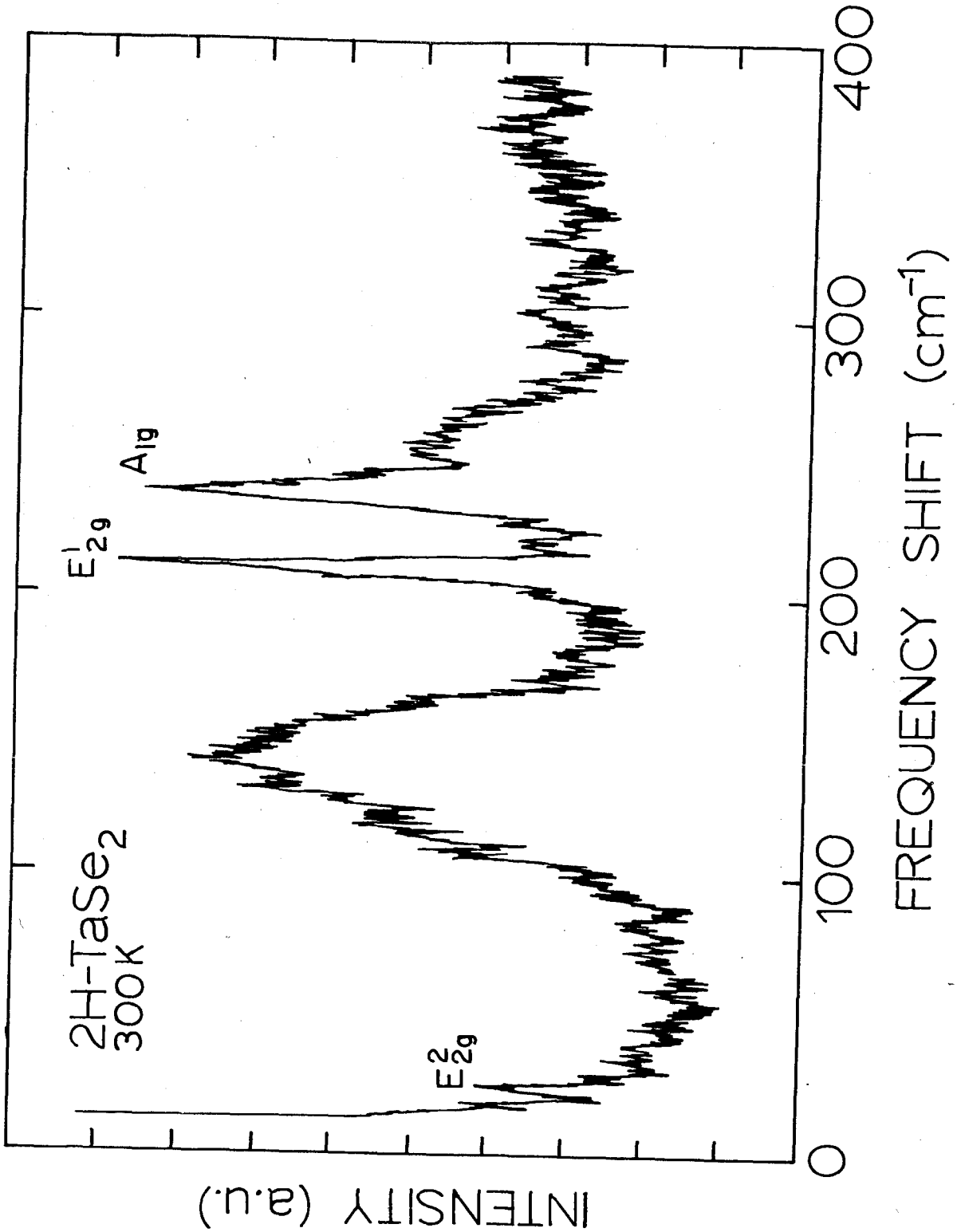

Figure 5.1 - Raman spectrum of 2H-$TaSe_2$ at 300K.

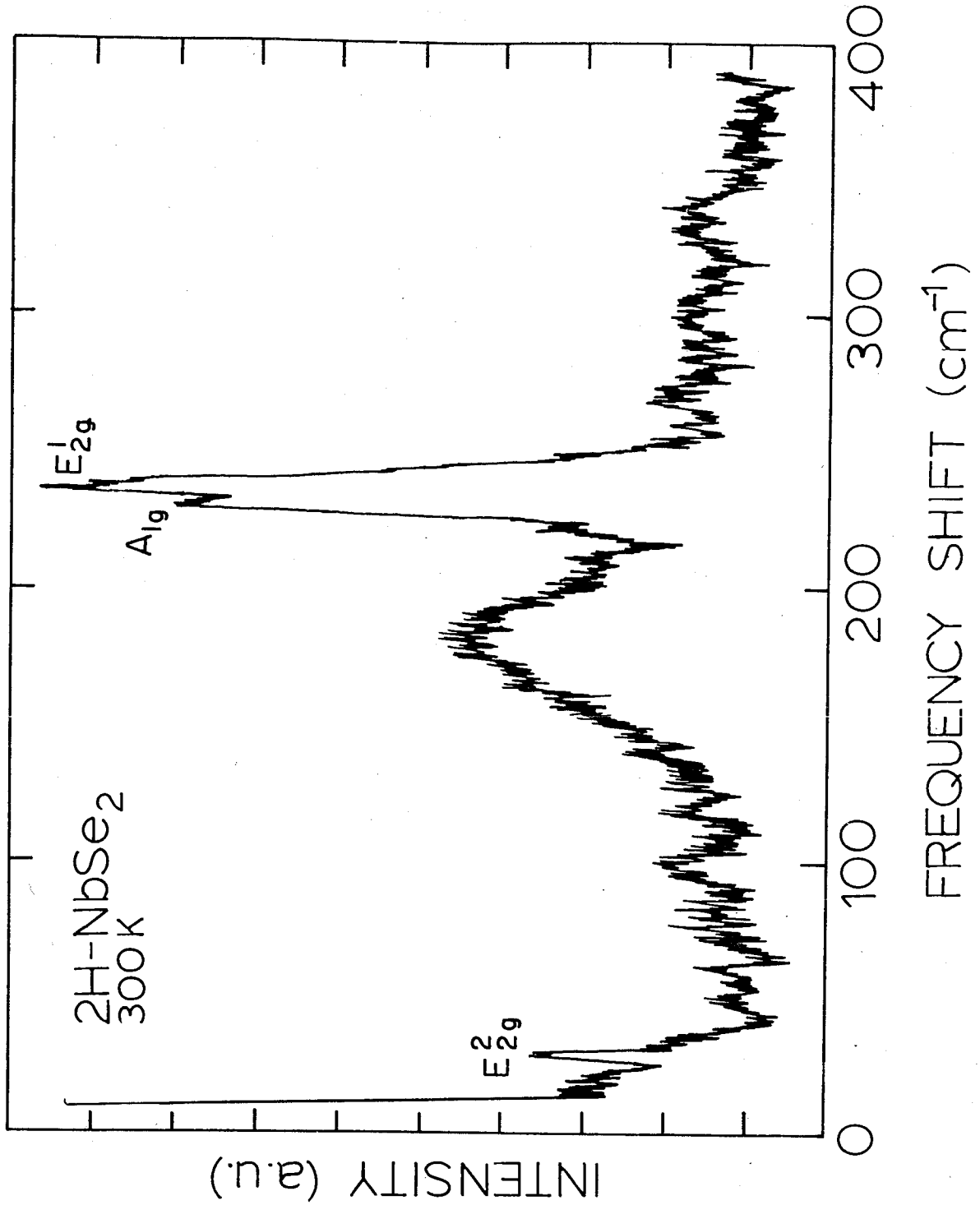

Figure 5.2 - Raman spectrum of 2H-$NbSe_2$ at 300K.

Mode	$TaSe_2$	$NbSe_2$	TaS_2	2H-NbS_2	Mode	3R-NbS_2
A_{1g}	234	231	400	379 ± 2	A_1^1	386 ± 2
E_{2g}^1	207	238	285	304 ± 3	E_2	330 ± 3
E_{1g}	139	133	230	260 ± 5	A_1^2	458 ± 3
E_{2g}^2	23	30	26	31 ± 2	E_1	290 ± 5

Table 5.1 - Frequencies (cm^{-1}) of Raman active phonons in group V transition metal dichalcogenides.

peak softens and is greatly reduced in intensity (Tsang et al. 1976, Holy et al. 1976). Below this temperature new Raman active modes appear which are associated with the formation of the CDW superlattice (Ibid.).

5.2 Tantalum Disulphide

Much less work has been reported for 2H-TaS_2 than for either $NbSe_2$ or $TaSe_2$. This is likely due to the poor optical quality of the crystal surface. The room temperature Raman spectrum is shown in Fig. 5.3. The E^2_{2g} rigid layer mode was observed using different instrumental settings than the rest of the scan in order to attenuate the Rayleigh scattered light. The E_{1g} peak cannot be seen on the spectra but Holy (1977) has tentatively identified it as a weak peak occurring at 230 cm^{-1}. The measured frequencies are listed in Table 5.1 and are in agreement with the findings of others (Holy 1977, Sugai et al. 1981)

The broad peak at 190 cm^{-1} is due to two-phonon scattering as in $TaSe_2$ and $NbSe_2$. Its temperature dependence, shown in Fig. 5.4, is also similar and shows a reduction in intensity and slight softening with decreasing temperature. From this behaviour coupled with the fact that 2H-TaS_2 also undergoes a CDW transition, it is expected that the LA phonon branch contains a Kohn anomaly analagous to $TaSe_2$ and $NbSe_2$. However this has not been seen directly because neutron diffraction experiments have yet to be reported for TaS_2.

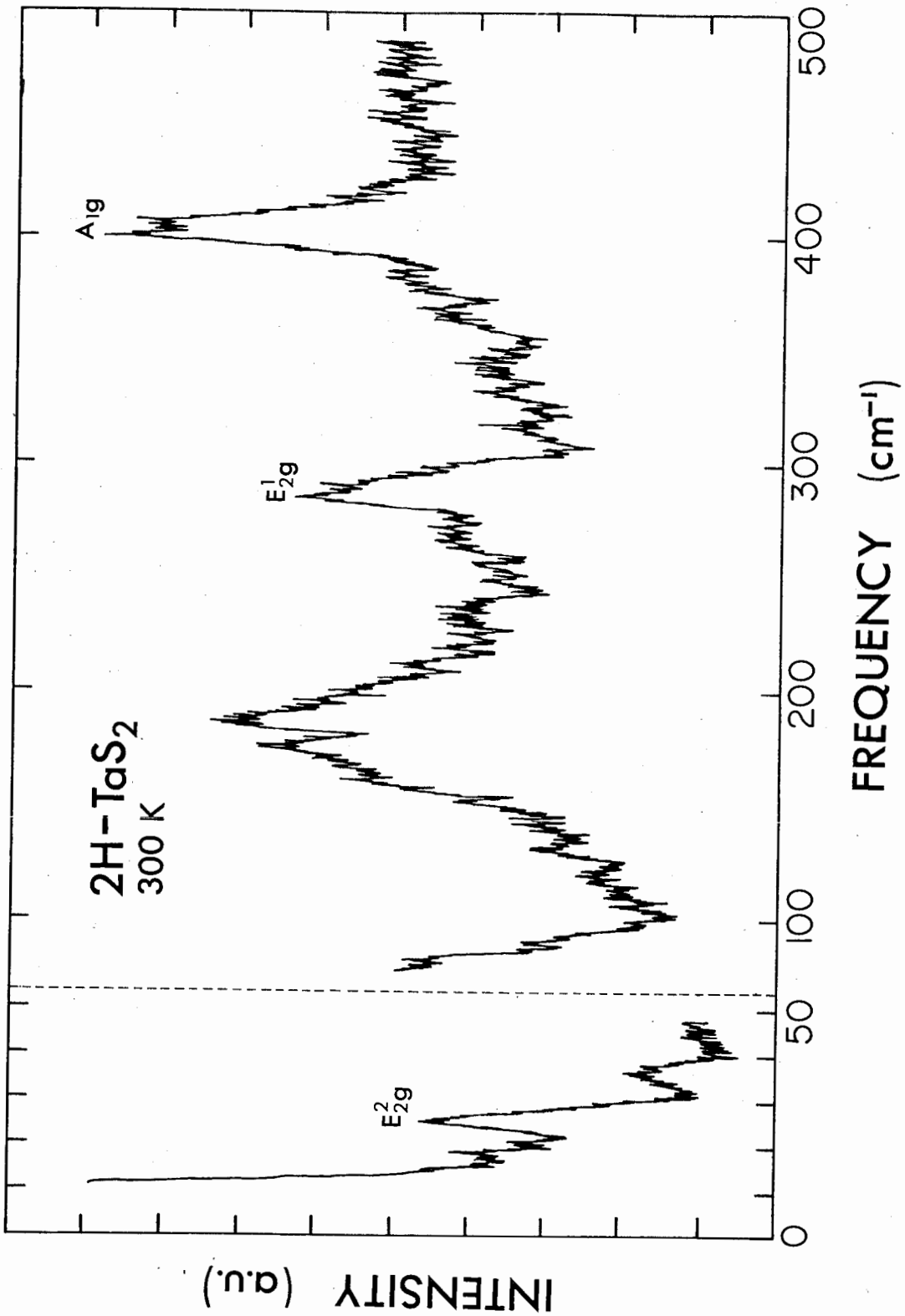

Figure 5.3 - Raman spectrum of 2H-TaS_2 at 300K.

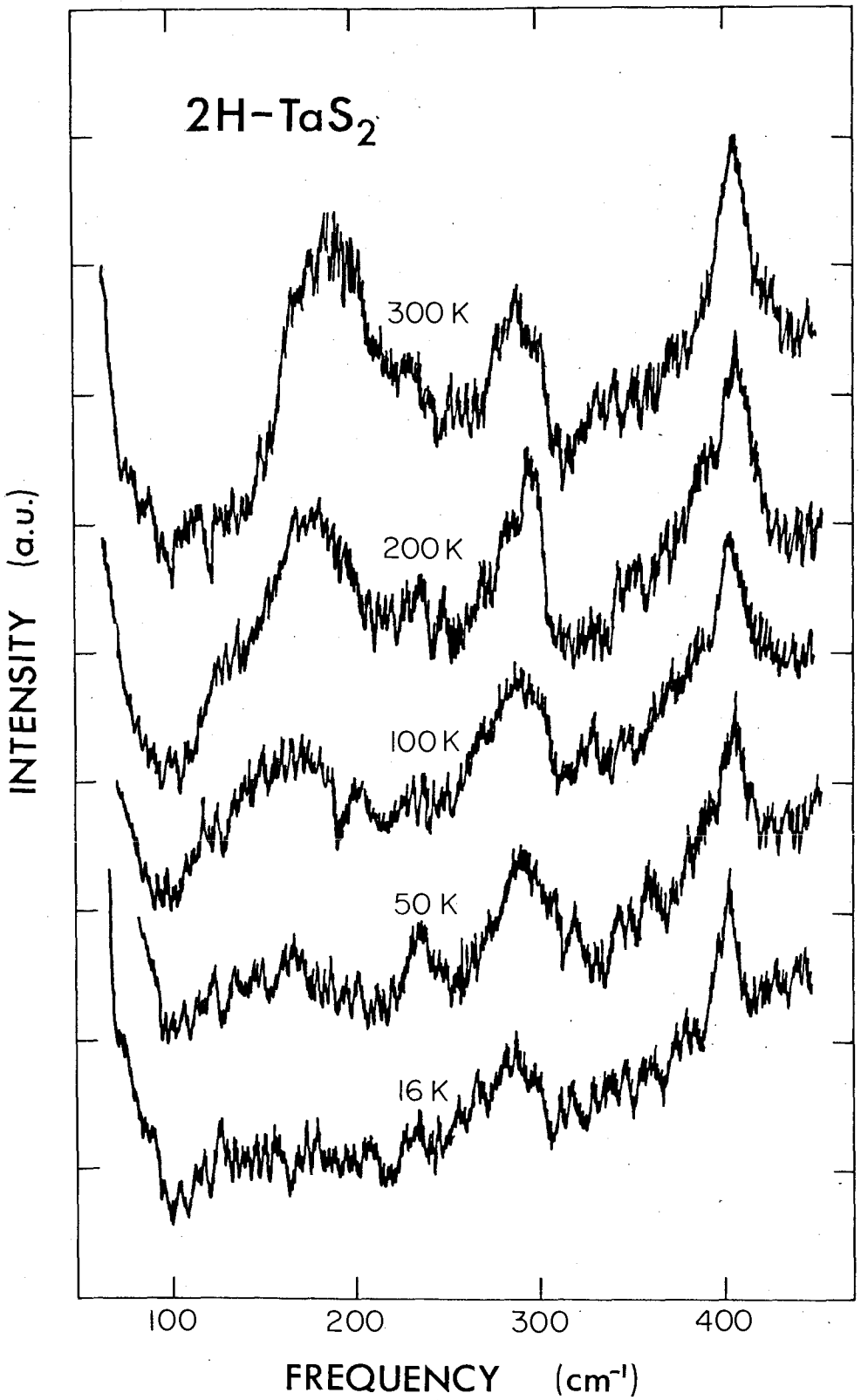

Figure 5.4 - Temperature dependence of Raman spectrum of 2H-TaS_2.

5.2 2H-Niobium Disulphide

An unpolarized spectrum of 2H-NbS_2 at room temperature is shown in Fig. 5.5. The E^2_{2g} rigid layer mode (shown in inset) can be clearly identified at 31 ± 2 cm^{-1}.

The broad feature at 290 cm^{-1} is characteristic of a two phonon peak. However, this is not believed to be the case for two reasons. First, on cooling to 15K the peak did not show a significant decrease in intensity relative to the other features as would be expected from the temperature dependence of a second order mode given in Table 2.2. Second, since 2H-NbS_2 does not undergo a CDW transition (Wilson et al., 1975) a strong second order feature similar to that observed in the other 2H compounds would not be expected.

Figure 5.6 shows NbS_2 spectra taken in XX and XY polarizations. Spectra with ZX and ZY polarizations were found to be qualitatively similar to the XX and XY spectra respectively which is attributed to the previously mentioned leakage (Sec. 4.3).

The broad peak is seen to be composed of two features, one of which, at 304 ± 2 cm^{-1}, is present on both scans. From Fig. 2.8 this is seen to be characteristic of an E_{2g} mode and is thus identified as E^1_{2g}. The sharp peak at 379 ± 2 cm^{-1} and the broader peak at 260 ± 5 cm^{-1} both have diagonal symmetry. The former can be identified as the A_{1g} mode on the basis of its similarity in width and intensity with the A_{1g} modes in $NbSe_2$, $TaSe_2$ and TaS_2.

The one remaining Raman active mode, E_{1g}, is assigned to the 260 cm^{-1} peak. The appearance of this mode in the XX spectrum is attributed to ZX leakage. In this context, and considering the weakness of the E_{1g} peak in

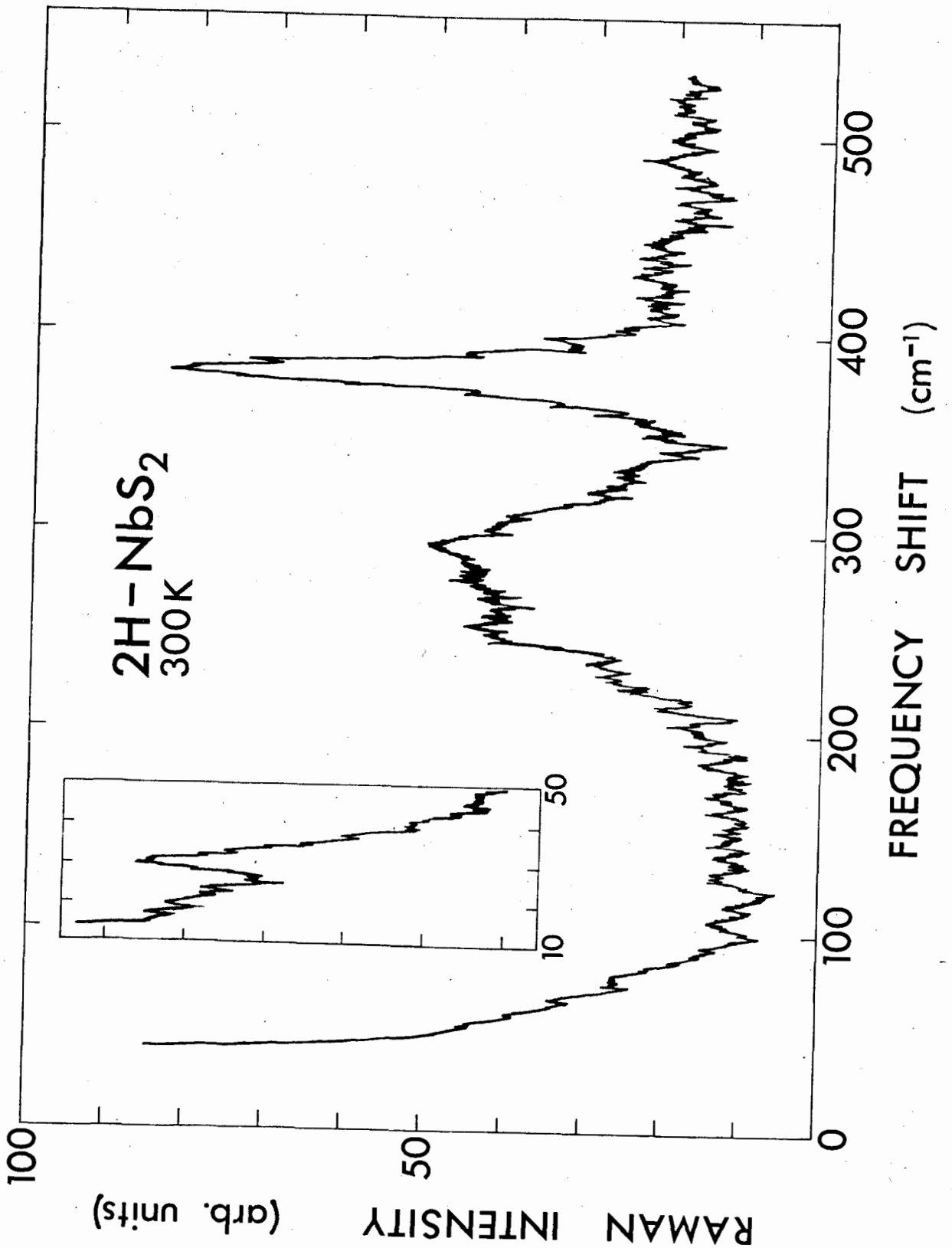

Figure 5.5 - Raman spectrum of 2H-NbS_2 at 300K.

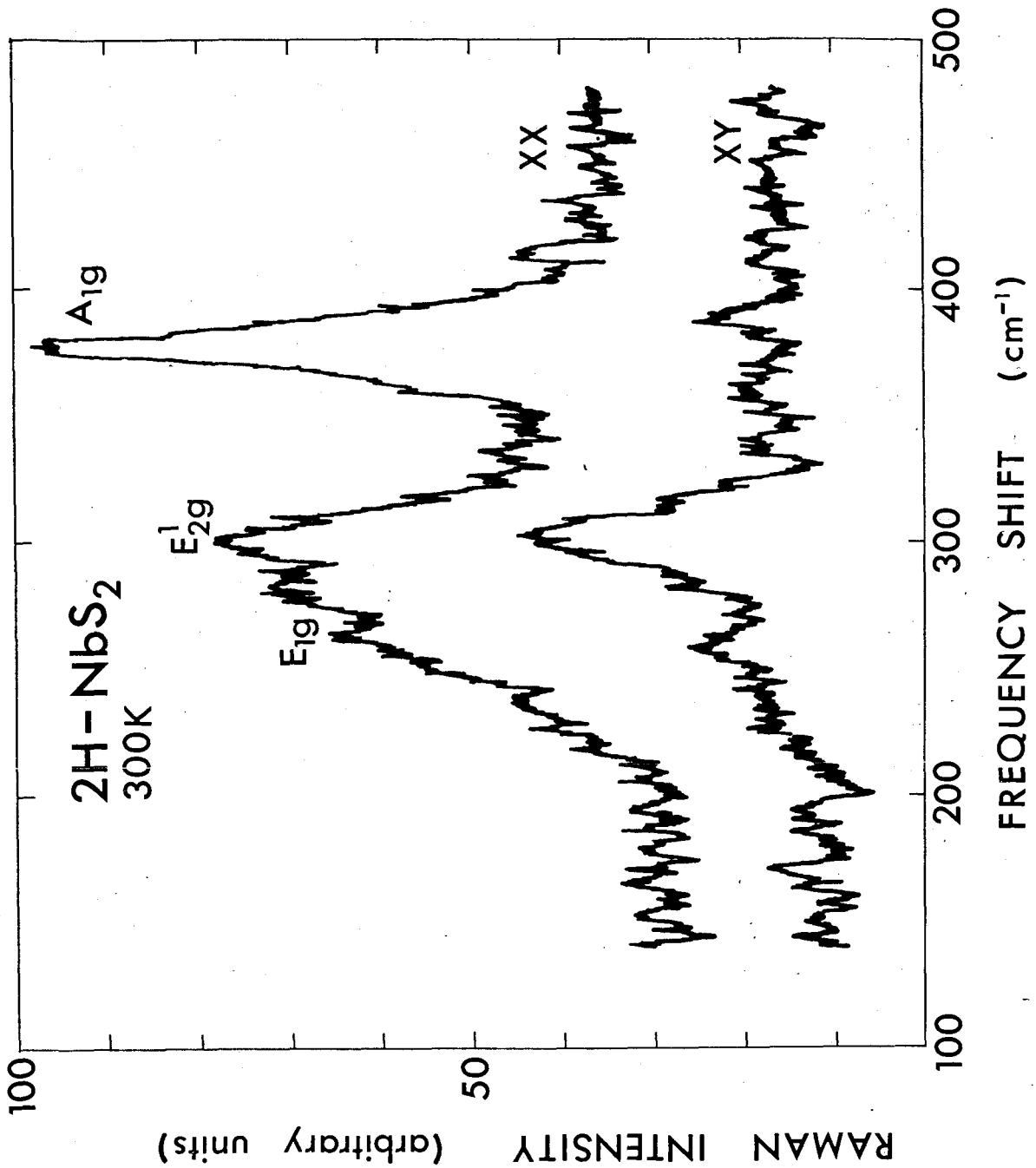

Figure 5.6 - Polarization dependence of 2H-NbS_2 Raman spectrum at 300K.

the other 2H compounds, this mode assignment must be considered very tentative.

5.4 3R-Niobium Disulphide

Raman spectra for 3R-NbS_2 in XX and XY polarizations at room temperature are shown in Fig. 5.7. The spectra were found to be independent of temperature on cooling to 15K which indicates that none of these features are due to two phonon processes.

From Fig. 5.7 it is clear that the strong peak at 386 ± 2 cm^{-1} is an A mode and is assigned thus. In addition the weaker peak at 458 ± 3 cm^{-1} also has diagonal symmetry and has been assigned as the second A_1 mode.

The two prominent features at 158 and 330 cm^{-1} as well as the 290 cm^{-1} shoulder all show polarization behaviour characteristic of an E mode and the symmetry assignments are less certain than for the case of the A modes. More conclusive evidence could be obtained from a ZZ polarization spectrum but such a spectrum could not be obtained because of the crystal dimensions. However, the identification can be made by a comparison with the 2H spectrum since the frequencies of the E modes should be approximately the same in the two polytypes (Verble and Weiting, 1970). This information leads to the assignment of the 290 and 330 cm^{-1} peaks as the two E modes.

It is possible that the 158 cm^{-1} peak is due to an impurity or defect mode, similar to that observed in impure $NbSe_2$ (Sooryakumar et al., 1981). Since this feature was observed in all of the 3R crystals studied it would appear likely that it is associated with the lack of stoichiometry inherent in 3R-NbS_2 (Fisher and Sienko, 1980).

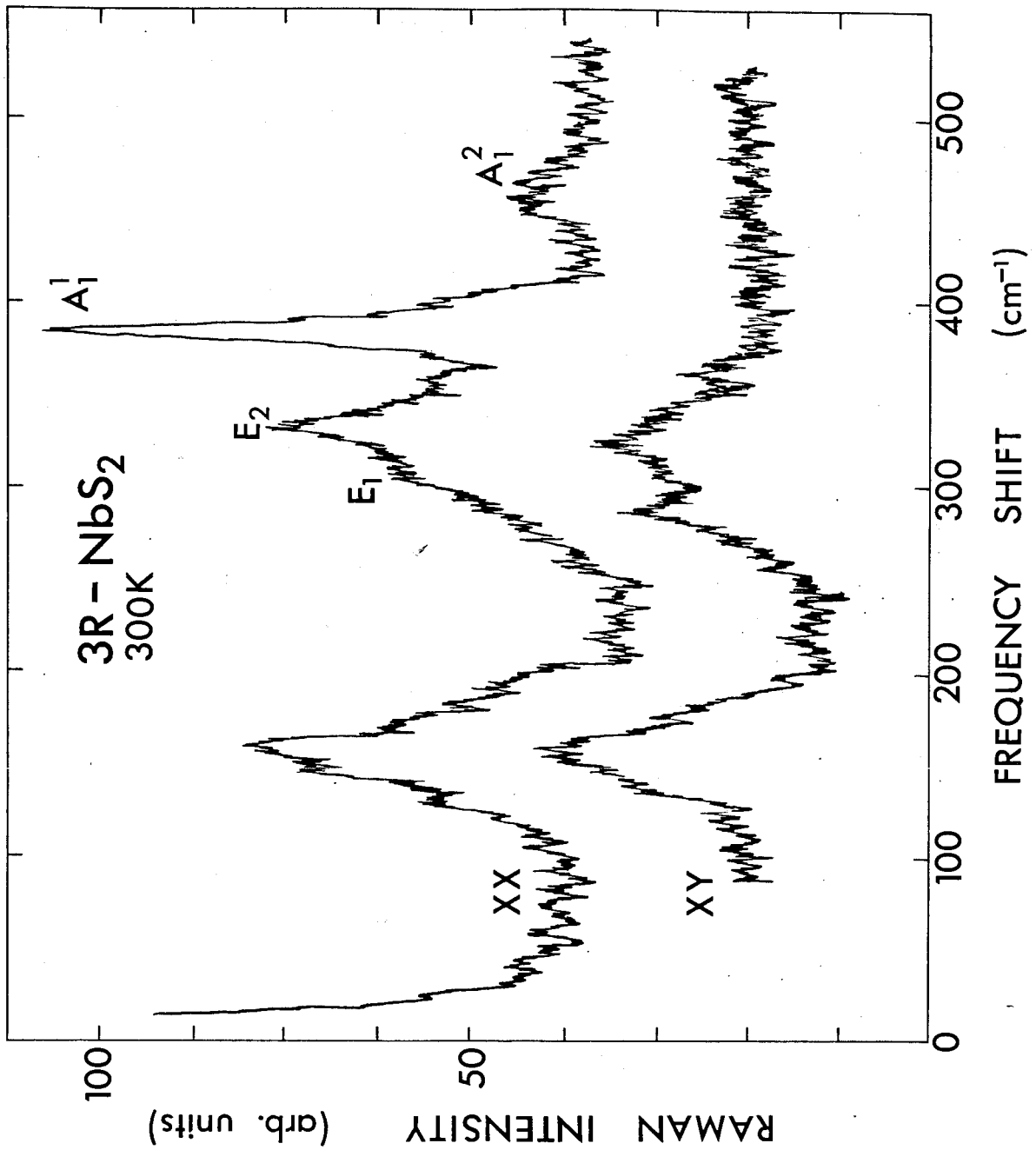

Figure 5.7 - Polarization dependence of 3R-NbS_2 Raman spectrum at 300K.

5.5 Comparison of 2H and 3R Niobium Disulphide Spectra

Upon examination of Figs. 2.4 and 2.6 it would be expected that the A_{1g} and A_1^1 modes would have approximately the same frequency and that the E_{2g}^1 should have a slightly higher frequency than the E_2 mode due to the interlayer coupling. From Table 5.1 it can be seen that the two A modes do indeed have reasonably similar frequencies but that the E_2 frequency is 25 cm^{-1} higher than that of the E_{2g}^1 mode!

An explanation of this apparent anomaly was put forward by Nakashima et al. (1982) who suggested that the predominant interlayer force could be due to interaction between the Nb atoms of one layer and the nearest S atoms of the adjacent layer. This seems unlikely however since it neglects interlayer nearest neighbour S-S interactions despite the fact that the S-S distance (3.44 A) is almost a full angstrom less than the Nb-S distance (4.42 A). Also, such an interlayer interaction is likely to be far too weak to cause a difference in frequency of more than a very few wavenumbers for these modes.

A more plausible explanation is the very probable enhancement of interlayer bonding in 3R-NbS_2 due to the excess Nb atoms situated in the van der Waals gap. The strength of a force constant describing a M-X (intralayer) bond is typically 20-100 times greater than the usual force constants associated with interlayer bonds. Thus, the presence of 10% excess Nb atoms, located in the gap, could conceivably account for the observed frequency difference.

5.6 Application of the VFF Model to Zone-centre Phonons

The VFF model described in Sec. 3.3 involves six parameters. However, for purposes of fitting the model to the experimental data of NbS_2 and TaS_2 only one interlayer force constant has been used. In addition, inspection of (3.3.2) shows that k_ϕ and k_θ always appear together and with the same coefficient (since $\theta = \phi$ in these compounds). Hence there are effectively only four parameters which have been used in fitting the data, namely k_r, k_{Rl}, k_ψ and $(k_\theta + k_\phi)$.

The force constants obtained by fitting the Raman data are given in Table 5.2. Although k_θ and k_ϕ appear as separate force constants, only their sum is meaningful. The force constants for $TaSe_2$ and $NbSe_2$ are those obtained by Feldman in fitting Raman, neutron and acoustic data for $TaSe_2$. The phonon frequencies obtained using these force constants in equations (3.3.2) are given in Table 5.3.

It was decided to exclude the E_{1g} mode from the fitting procedure for 2H-NbS_2 based on the somewhat uncertain nature of its experimental determination. Instead the 458 cm^{-1} A_1^2 mode observed in 3R-NbS_2 was fit to the A_{2u} mode in 2H-NbS_2. These two A modes can be expected to have nearly the same frequency based on the similarity of their vibrations (Figs. 2.4 and 2.6) and the experimentally observed similarity of the A_{1g} and A_1^1 modes. Although all four of the 2H-NbS_2 Raman modes can be as equally well fit as the four modes chosen, and in fact the four 2H-NbS_2 Raman modes as well as the A_{2u} mode can be simultaneously fit to better than 6%, the resulting force constants did not seem to be in keeping with those of the other compounds or with those of MoS_2 obtained from a very similar model (Wakabayashi et al., 1975). This stems from the difficulty of trying to fit the E_{1g} mode, which, if the model can be used as a criterion, seems to

	TaS_2	NbS_2	$TaSe_2$	$NbSe_2$
k_r	0.77	0.79	0.74	0.74
k_{R1}	0.053	0.0475	0.0377	0.0377
k_{R2}	-	-	0.0137	0.0137
k_ψ	0.1	0.05	0.1	0.1
k_θ	0.2	0.178	0.078	0.078
k_ϕ	0.2	0.178	0.1892	0.1892

Table 5.2 - Force constants for 2H compounds (10^5 dyn/cm)

Mode	TaS_2		NbS_2		$TaSe_2$		$NbSe_2$	
	Model	Expt.	Model	Expt.	Model	Expt.	Model	Expt.
A_{1g} (R)	400	400	379	379	232	234	231	231
E^1_{2g} (R)	283	285	305	304	198	207	236	238
E_{1g} (R)	232	230	231	260?	139	139	139	133
E^2_{2g} (R)	26	26	31	31	24	23	29	30
A_{2u} (IR)	420	-	458	458*	281	-	336	-
E_{1u} (IR)	279	-	303	-	196	-	235	-
B^1_{2g} (I)	430	-	465	-	285	-	338	-
B_{1u} (I)	385	-	365	-	223	-	222	-
E_{2u} (I)	227	-	226	-	134	-	134	-
B^2_{2g} (I)	54	-	64	-	43	-	49	-

* - Based on frequency of A^2_1 mode in 3R-NbS_2 (see text).

Table 5.3 - Frequencies of zone centre phonons in 2H compounds. Optical activity shown in brackets.

to cast further uncertainty on the validity of the E_{1g} frequency.

In an effort to determine k_θ and k_ϕ for TaS_2, an attempt was made to simultaneously fit the four Raman modes and the initial slope of the LA dispersion curve. The slope has been measured with ultrasonic techniques (Jericho et al., 1980). Unfortunately this proved unsuccessful and only the four Raman modes were fit. The problem with trying to fit the initial slope is attributable to the fact that long wavelength acoustic phonons are likely to involve forces of a long range nature whereas the model contains only short range forces. The speed of sound, calculated from the initial slope as predicted by the model, is 4.7×10^5 cm/s. The measured value is 3.6×10^5 cm/s.

There are apparently no other experimental results with which the validity of the model can be tested. Measurement of the frequencies of the IR active phonons, which can be easily compared to equations (3.3.2), will probably be the best independent check of the models predictive ability.

The full dispersion curves for TaS_2 and NbS_2, based on the force constants of Table 5.2, are presented in the next chapter and in Appendix II.

VI. Results and Discussion - Intercalated Crystals

6.1 Results

Approximately 30 samples of Ag_xTaS_2 were studied with concentrations ranging from $0.10 \lesssim x \lesssim 0.67$ and temperatures ranging from 15-300K. In general these samples showed no structure in the Raman spectrum, likely because of the very poor surface quality. However, in four of the samples studied, with concentrations of x = .13, .26, .28, and .32, three new Raman active modes were observed.

The spectrum of $Ag_{.28}TaS_2$ is depicted in Fig. 6.1. It should be mentioned that the signal-to-noise ratio in this spectrum is far higher than that typically observed in these compounds. The three new peaks are observed at 320, 335, and 427 cm^{-1}. The peak at 400 cm^{-1} is the only apparent feature surviving from the pure crystal.

Because of the generally poor quality of the spectra obtained from these intercalation compounds, any quantitative information other than the frequencies was difficult to obtain. However a rough estimate of the temperature dependence of the modes in $Ag_{.28}TaS_2$ may be obtained from Fig. 6.2. At 15K (Fig. 6.1) and 40K (not shown) all peaks were clearly defined. As the temperature was raised, the 320 and 335 cm^{-1} modes were seen to dissappear between about 130 and 160K while the 427 cm^{-1} peak remained until somewhere between about 160 and 190K. (All temperatures quoted do not take laser heating into account). Surprisingly the 400 cm^{-1} mode, which should be present up to 300K, disappeared into noise at approximately 200K. Spectra from the other three samples which showed these three new modes

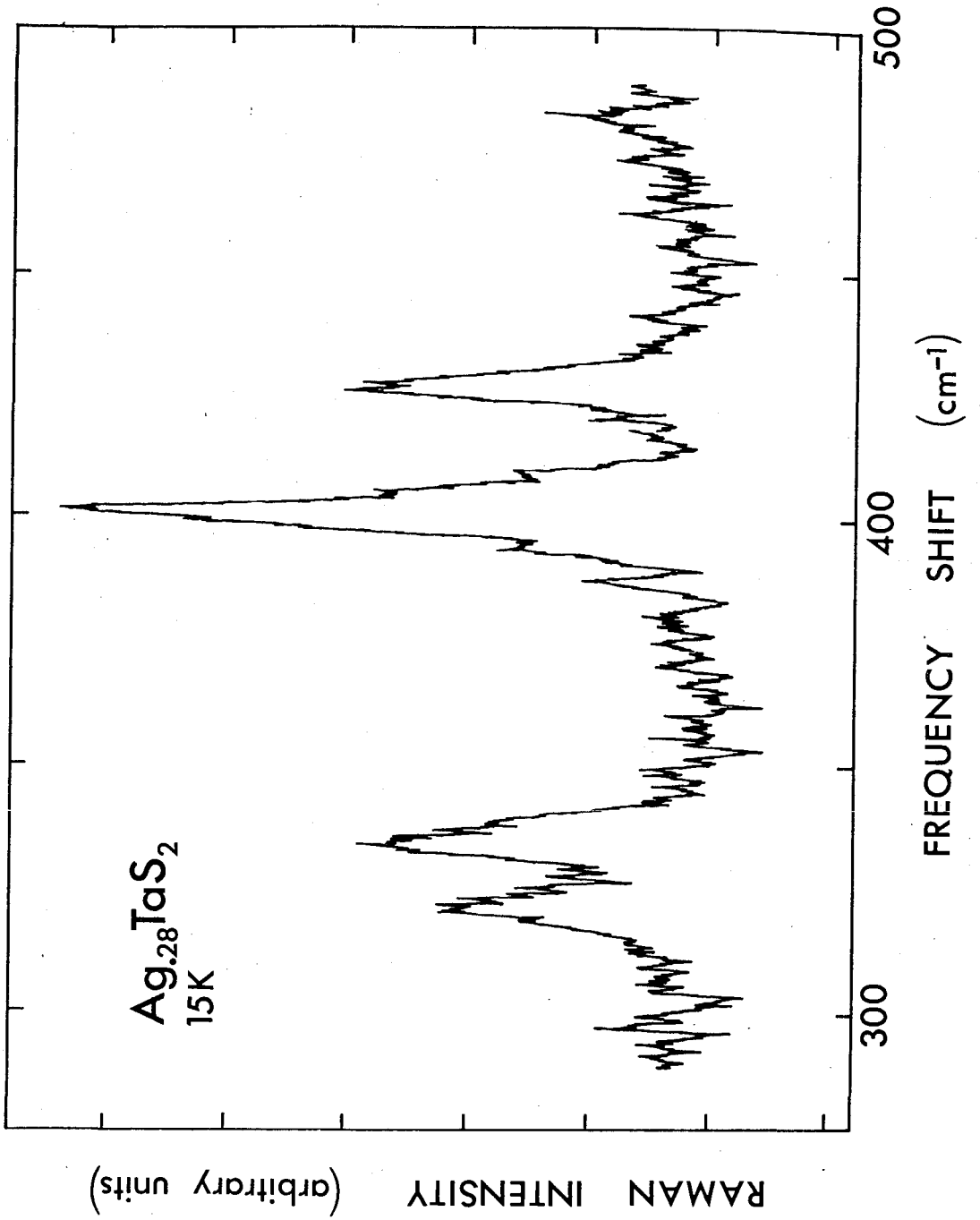

Figure 6.1 - Raman spectrum of $Ag_{.28}TaS_2$ at 15K.

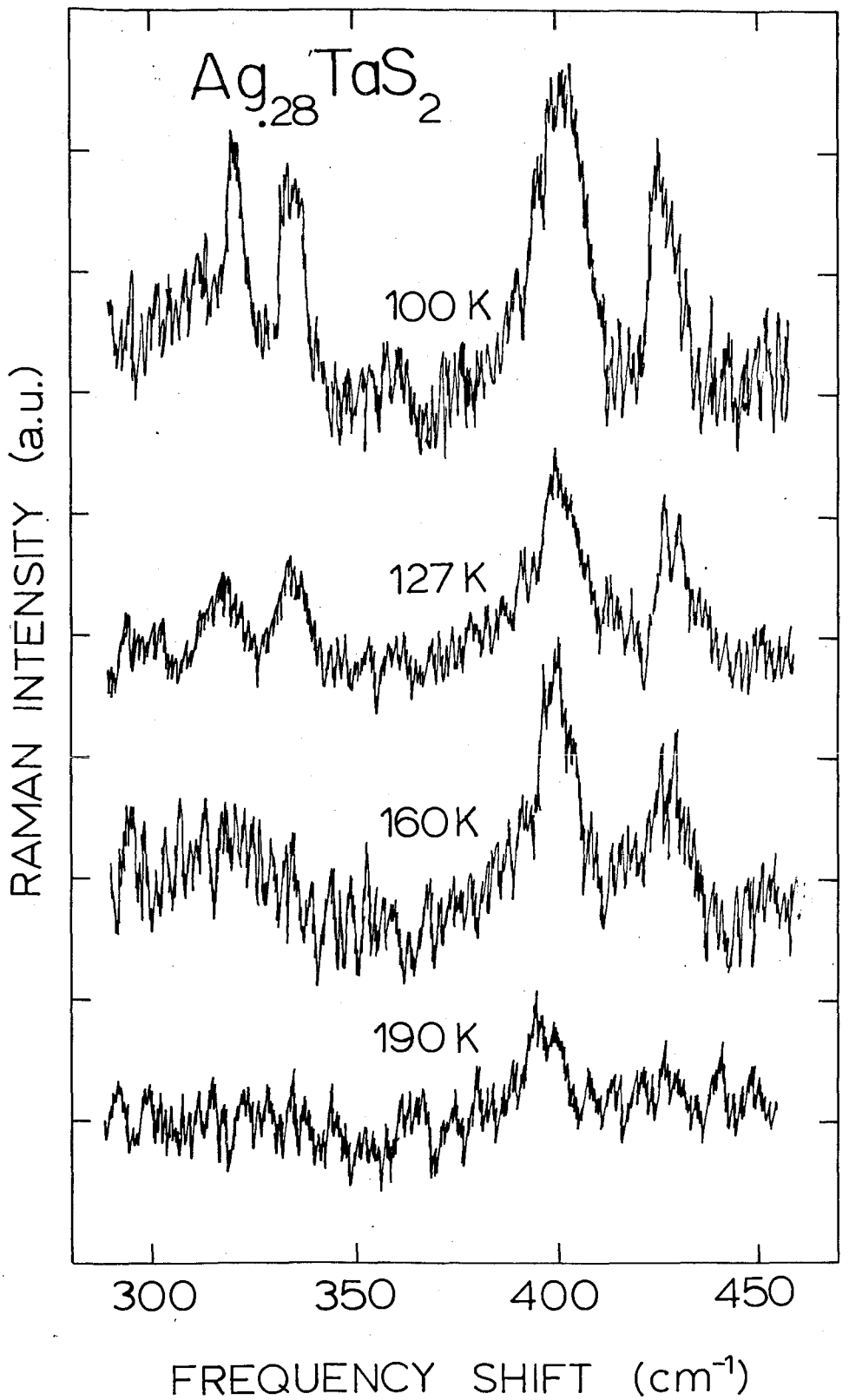

Figure 6.2 - Temperature dependence of Raman spectrum of $Ag_{.28}TaS_2$.

were obtained at temperatures less than 80K.

Polarization checks of the modes in Fig. 6.1 showed that all four had A (diagonal) symmetry.

Despite investigation of several intercalated crystals with concentrations $1/3 \leq x \leq 2/3$, and in particular with $x = 2/3$, no spectra could be obtained.

6.2 Discussion

The formation of a CDW has been reported for Ag_xTaS_2 with $x \leq 1/4$ and with a transition temperarure of about 76K (Scholz et al., 1982b). However the three new Raman modes are not beleived to be associated with the CDW since they have been observed well above the transition temperature. Instead it is felt that they are result of zone-folding caused by the formation of a superlattice arising from the ordering of the intercalate atoms. Similar zone-folded Raman active phonons have been observed in other intercalated materials (Leonelli et al. 1980, Wada et al. 1981, Plischke et al., to be published).

An extensive study on the formation of superlattices in Ag_xTaS_2 has been reported (Scholz et al., 1982a and 1982b). This study, undertaken using electron diffraction, showed that the type of superlattice formed was a rather complex function of both temperature and silver concentration. The results are summarized in Table 6.1 (after Scholz et al., 1982b).

The experimentally observed temperature and silver concentration dependence of the new Raman modes can be correlated with the superlattice variations observed by Scholz et al. (Table 6.1) and thus should determine the type of superlattice present in the Raman samples. This in turn indicates from which point zone-folding can be expected to occur or,

x	stage	Superlattices Observed			
		about 400K to 300K	about 300K to 200K	about 200K to 100K	about 100K to 25K
zero	-	-	-	-	"$3a_o$" CDW/PLD $(0.338\pm0.002)a_o^*$
zero to ∿1/6	Properties correspond to a mix of those for x = zero and x = 1/6. No observable change in q* of the CDW/PLD. Sometimes very weak $2a_o$ superlattice satellites are observed.				
1/6 (ideal behaviour)	2	$\sqrt{3}a_o$	$\sqrt{3}a_o$	$\sqrt{3}a_o$	$\sqrt{3}a_o$; "$3a_o$" CDW/PLD $(0.337\pm0.002)a_o^*$
∿1/6 to ∿1/3	Properties are a mix of those for x = 1/6 and x = 1/3, with those of the latter becoming more apparant at lower temperatures. The "$3a_o$" CDW/PLD superlattice is lost just above x = ¼ where it is $(0.347\pm0.002)a_o^*$.				
1/3	2	-	$2a_o$	$2a_o$	$2a_o$; $(5\sqrt{3}\times2)a_o$
∿1/3 to ∿2/3	Properties are a mix of those for x = 1/3 and 2/3, with those of the latter predominating at lower temperatures. For x ≃ ½ in the stage 1 regions, the low temperature superlattice is $(2\sqrt{3}\times3)a_o$ and not $(2\sqrt{3}\times5)a_o$ as expected.				
2/3	1	-	$(\sqrt{3}\times2)a_o$ and absences k = odd	$(\sqrt{3}\times2)a_o$	$(\sqrt{3}\times2)a_o$; $(2\sqrt{3}\times5)a_o$

Table 6.1 - Observed superlattices in Ag_xTaS_2 (after Scholz et al., 1982b).

equivalently, from which point in the Brillouin zone the new Raman modes originate. Since these modes have not been observed for $x > 1/3$ it is assumed that they are not related to the $(\sqrt{3}x2)a_o$ or $(2\sqrt{3}x5)a_o$ superlattices (or their 'orientational variants') which are observed at these concentrations. In addition, since they have been observed up to about 150K, it is expected that are not associated with the $(5\sqrt{3}x2)a_o$ superlattice (and its orientational variants) which forms at $T \lesssim 100K$ in $Ag_{1/3}TaS_2$.

The only superlattice present at all temperatures in $Ag_{1/3}TaS_2$ is $2a_o$. For $1/4 \lesssim x \lesssim 1/3$ the room temperature superlattice is $\sqrt{3}a_o$ but upon cooling a $2a_o$ superlattice also appears. Although the $2a_o$ superlattice is weaker than the $\sqrt{3}a_o$, particularly at lower concentrations, the first appearance of the $2a_o$ superlattice is reported at 230K for $x = .26$ and 180K for $x = .13$. This roughly corresponds to the temperature at which the new Raman modes appear and thus it seems plausible that the new modes are associated with the $2a_o$ superlattice. However, zone-folding from the K point due to the formation of the $\sqrt{3}a_o$ superlattice certainly cannot be ruled out.

Still a third possibility is presented by considering the fact that the new modes have been observed only in stage 2 compounds (ie. $x \lesssim 1/3$) and not for stage 1. X-ray diffraction studies (Scholz and Frindt, 1980) of $Ag_{1/3}TaS_2$ (stage 2) and $Ag_{2/3}TaS_2$ (stage 1) show that while the c-axis triples to accomodate six layers per unit cell in the stage 2 compound, it remains essentially unchanged in the case of stage 1. Hence zone-folding is also quite possible from points along the Δ symmetry direction. In particular, it can be expected to occur from a point 2/3 along the line ΓA.

In an attempt to check the origin of the new modes, phonon dispersion curves for pure TaS_2, based on the VFF model and the force constants of Table 5.2, have been plotted along ΓA, ΓM and ΓK. These are shown in Figs. 6.3a and 6.3b.

The assumption is made that the intercalate atoms in Ag_xTaS_2 serve only to change the periodicity of the host lattice and do not affect the phonon frequencies. Under this assumption the frequencies should correspond to the frequencies calculated at M, K or 2/3 ΓA.

Figures 6.3a and 6.3b indicate that the 427 cm^{-1} peak originates from zone-folding along the uppermost Δ_1 or Δ_2 branches which, at 2/3 ΓA, have frequencies of 428 and 423 cm^{-1} respectively.

The origin of the 320 and 335 cm^{-1} peaks is not as clear. It does appear that they do not originate from Δ points since, from Fig. 6.3a, there are no phonons along ΓA with frequencies at all close to 320 or 335 cm^{-1}. However, whether these two modes are a result of zone-folding from M or K is uncertain. A first glance at Fig. 6.3 indicates that zone-folding is most likely to occur from K where the uppermost T_3 branches are degenerate with a frequency of 325 cm^{-1}. In contrast, at M, the phonons with frequencies of 302 and 344 cm^{-1} are the closest in frequency to those of the two new Raman modes. Unfortunatley however, no firm conclusions can be reached as there still exists considerable uncertainty - this is principly due to the fact that the force constants k_θ and k_ϕ are indeterminate but which both have effects on the dispersion of the optic branches. For example, by choosing $k_\theta \simeq 0.3$ and $k_\phi \simeq 0.1$, which keeps the zone centre frequencies unchanged, the 320 and 335 cm^{-1} frequencies can be simultaneously matched to within about 3 cm^{-1} of frequencies at either the K or M points. However such a value for k_θ is felt to be too large when compared to Feldman's value (Table 5.2) or that of Wakabayashi et al.

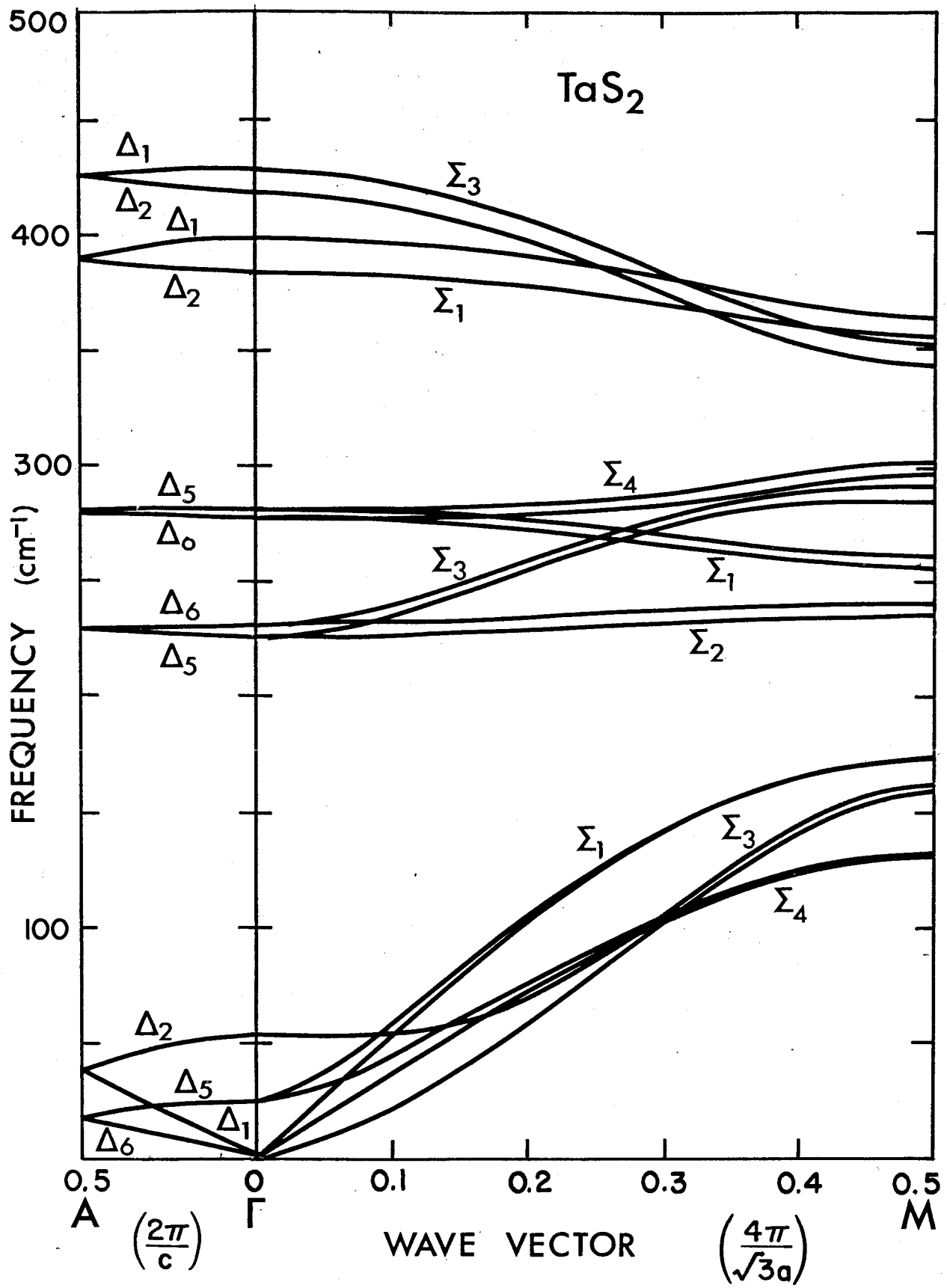

Figure 6.3a - Phonon dispersion curves of 2H-TaS_2 along ΓA and ΓM (based on VFF model).

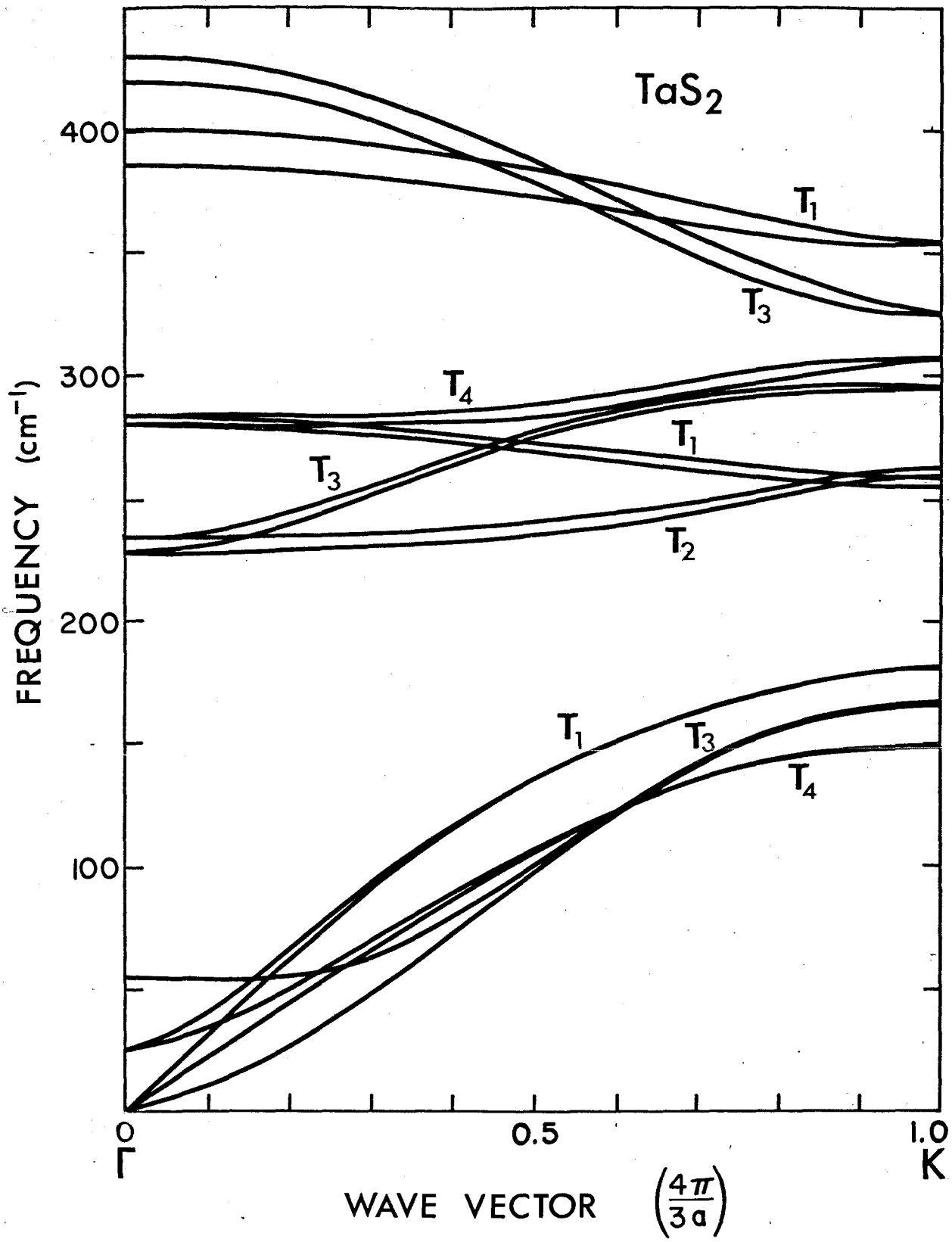

Figure 6.3b - Phonon dispersion curves of 2H-TaS_2 along ΓK (based on VFF model).

(1975) for MoS_2. Further data will be required before a determinate statement can be made about the origin of these two peaks.

VII. Concluding Remarks

7.1 Summary

A valence force field model has been used to assist in the investigation of the lattice dynamics of layered compounds. Explicit expressions for the zone centre phonon frequencies of the 2H compounds have been obtained from the model and these expressions, along with the experimentally measured Raman frequencies, were used to evaluate the force parameters of the model for 2H-TaS_2 and 2H-NbS_2. Using these parameters, the phonon dispersion curves for TaS_2 were plotted and later used to interpret the Raman spectrum of Ag_xTaS_2.

The frequencies of all the Raman active phonons predicted by group theory were measured for 2H-NbS_2 and 3R-NbS_2. The frequencies were found to be 290 cm^{-1} (E_1), 330 cm^{-1} (E_2), 386 cm^{-1} (A_1^1), and 458 cm^{-1} (A_1^2) for 3R-NbS_2 and 31 cm^{-1} (E_{2g}^2), 304 cm^{-1} (E_{2g}^1), 379 cm^{-1} (A_{1g}) and 260 cm^{-1} (E_{1g}) for 2H-NbS_2 although the latter frequency is still somewhat uncertain. Only the E_2, A_1^1, A_{1g} and E_{2g}^1 frequencies had been previously reported.

The Raman spectrum of Ag_xTaS_2 (for $x \lesssim 1/3$) was measured and found to contain three modes not present in the pure crystal. The new modes had frequencies of 320, 335 and 427 cm^{-1}. All three modes only become evident below temperatures of about 150-200K and all possessed diagonal symmetry characteristic of an A mode.

The appearance of these new modes was attributed to a zone-folding mechanism due to the formation of a superlattice caused by the presence of

ordered intercalates. The phonon dispersion curves for TaS_2 were used in an effort to determine the origin of the zone-folded phonons. The results indicated that the 427 cm^{-1} peak was due to zone-folding along the c^* axis. The origin of the other two modes is not as clear but the two most likely locations are the K and M points of the Brillouin zone.

7.2 Suggestions for Future Investigations

The 2H and 3R polytypes of NbS_2 appear to possess properties that should make it a system of interest to both experimentalist and theoretician and worthy of further study.

A very basic question that remains to be answered is why 2H-NbS_2 lacks a CDW but perhaps a more intriguing question is the effect of excess Nb atoms on the physical properties of NbS_2. A very preliminary investigation of the Raman spectrum of apparently pure 2H-NbS_2 has shown that as the temperature is decreased from room temperature the spectrum changes very noticeably, becoming similar to that of 3R-NbS_2. This behaviour is reproducible and reversible and suggests a 2H - 3R structural phase transition in $Nb_{1+x}S_2$. The existence of such a transition could be clarified by doing X-ray structural analysis at different temperatures on $Nb_{1+x}S_2$ samples of known x. It would also be of interest to conduct Raman scattering experiments on NbS_2 intercalated with Ag, Cu, Fe, etc. not only for general interest but to determine whether there is any difference between the presence of intercalate atoms or excess Nb atoms in the van der Waals gap.

In the case of unintercalated 2H and 3R-NbS_2, it would be worthwhile to perform a detailed calculation of the interlayer bonding enhancement in 3R-NbS_2 to determine whether the excess Nb atoms can account for the

frequency difference between the E_2 and E^1_{2g} modes or whether another mechanism is responsible.

In the absence of any IR or neutron data the VFF model can be further refined by performing a two-phonon density of states calculation and correlating the results to the observed two phonon peak in the Raman spectrum of TaS_2. This should enable a determination of all the force constants in the model lending more confidence to the phonon dispersion curves and likely resolving the question of whether zone-folding occurs from the M or K point in Ag_xTaS_2.

Finally, the model might be used to interpret the Raman spectra of very thin crystals of NbS_2 and TaS_2. Such crystals, at most only a very few layers thick, have been examined and new features in the Raman spectra have been observed. Density of states calculations based on the model could possibly determine whether the new features are related to the finite thickness of these crystals, in an analagous manner to that reported for microcrystallites of graphite (Nemanich and Solin, 1979).

Appendix I - Procedure Used to Construct Dynamical Matrix

Expressing Δr in terms of cartesian position vectors and atomic displacements is straightforward:

$$\begin{aligned} \Delta r &= |\vec{r}_i' - \vec{r}_j'| - |\vec{r}_i - \vec{r}_j| \\ &\simeq \frac{1}{r}(\vec{r}_i - \vec{r}_j)\cdot(\vec{u}_i - \vec{u}_j) \end{aligned} \tag{A1.1}$$

to first order in $|\vec{u}|$. The primes denote non-equilibrium position vectors as shown in Fig. A1.1a and the subscripts i, j, k are used instead of the more conventional K, K'.

The starting point in evaluating $\Delta\theta$ is to take

$$\begin{aligned} \Delta(\cos\theta) &= \sin\theta\,\Delta\theta \\ &= \cos\theta' - \cos\theta \end{aligned} \tag{A1.2}$$

where, with reference to Fig. A1.1b,

$$\cos\theta' = \frac{(\vec{r}_i' - \vec{r}_j')\cdot(\vec{r}_k' - \vec{r}_j')}{|\vec{r}_i' - \vec{r}_j'|\;|\vec{r}_k' - \vec{r}_j'|} \tag{A1.3}$$

and

$$\cos\theta = \frac{(\vec{r}_i - \vec{r}_j)\cdot(\vec{r}_k - \vec{r}_j)}{|\vec{r}_i - \vec{r}_j|\;|\vec{r}_k - \vec{r}_j|} \tag{A1.4}$$

Here the convention has been adopted that the subscript 'j' refers to the apex atom of the bond. For the 2H-MX_2 compounds, all angles appearing in

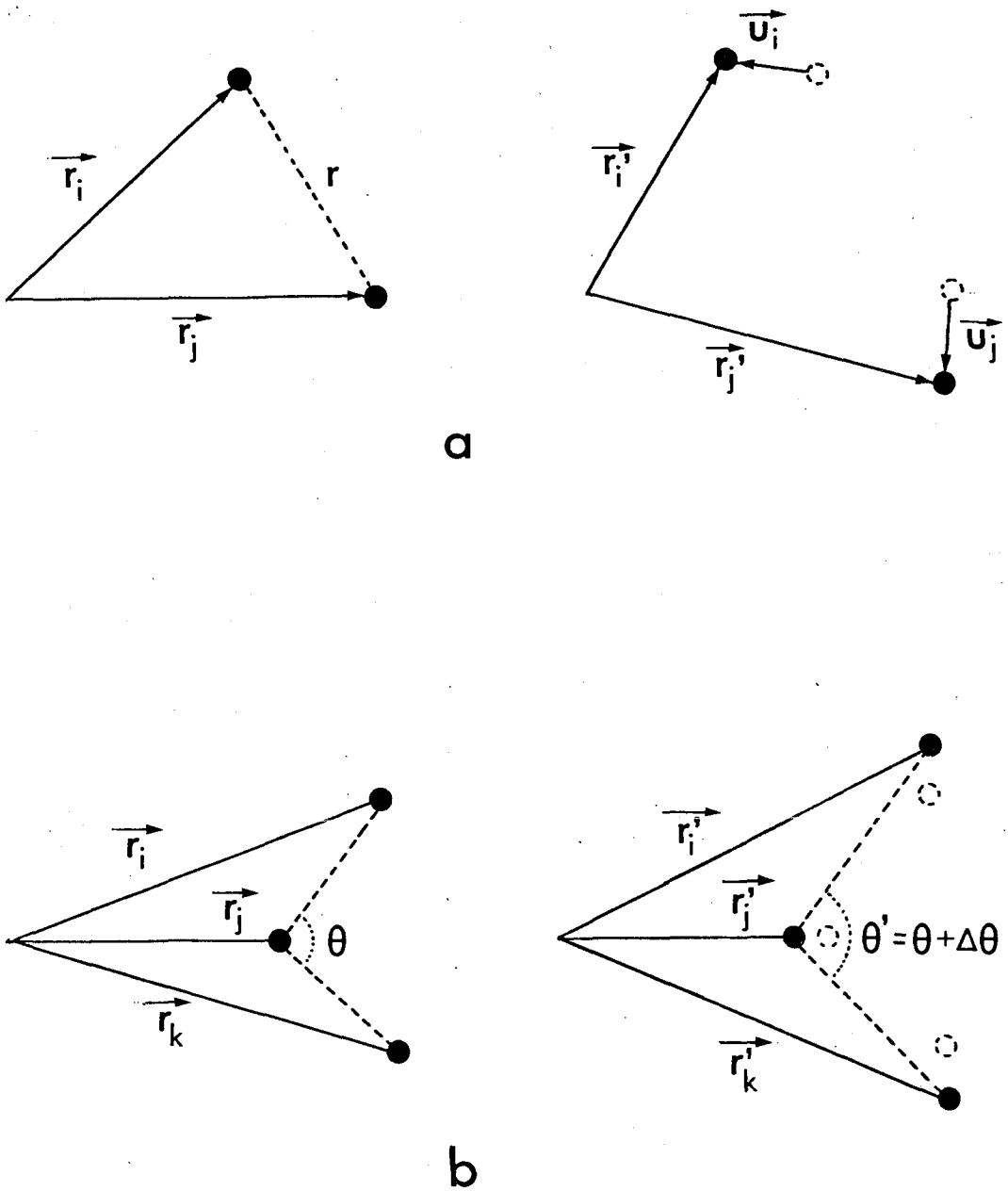

Figure A1.1 - Diagrams used to express a) Δr and b) $\Delta\theta$ in terms of cartesian position vectors and displacements. Primes denote non-equilibrium positions.

(3.3.1) are approximately 80° hence the $\sin\theta$ term in (A1.2) can be taken as unity. Using this approximation along with (A1.3) and (A1.4) in (A1.2) and keeping only terms to first order in $|\vec{u}|$ yields

$$\Delta\theta \simeq \frac{1}{r^2}\left[\left(\vec{R}_{ij}\cdot\vec{u}_{ij} + \vec{R}_{kj}\cdot\vec{u}_{kj}\right)\cos\theta - \left(\vec{R}_{ij}\cdot\vec{u}_{kj} + \vec{R}_{kj}\cdot\vec{u}_{ij}\right)\right] \qquad \text{(A1.5)}$$

where $\vec{R}_{ij} \equiv \vec{r}_i - \vec{r}_j$ and $\vec{u}_{ij} \equiv \vec{u}_i - \vec{u}_j$. Using (A1.1) and (A1.5), the general expression for the bond stretching and bond angle bending terms appearing in the potential energy (3.3.1) are

$$\frac{1}{2}k_r(\Delta r)^2 = \frac{1}{2}k_r\frac{1}{r^2}\left[\vec{R}_{ij}\cdot\vec{u}_{ij}\right]^2 \qquad \text{(A1.6)}$$

and

$$\frac{1}{2}k_\theta(r\Delta\theta)^2 = \frac{1}{2}k_\theta\frac{1}{r^2}\left[\left(\vec{R}_{ij}\cdot\vec{u}_{kj} + \vec{R}_{kj}\cdot\vec{u}_{ij}\right)^2 - 2\cos\theta\left(\vec{R}_{ij}\cdot\vec{u}_{ij} + \vec{R}_{kj}\cdot\vec{u}_{kj}\right)\left(\vec{R}_{ij}\cdot\vec{u}_{kj} + \vec{R}_{kj}\cdot\vec{u}_{ij}\right) + \cos^2\theta\left(\vec{R}_{ij}\cdot\vec{u}_{ij} + \vec{R}_{kj}\cdot\vec{u}_{kj}\right)^2\right] \qquad \text{(A1.7)}$$

A particular unit cell is chosen and all interactions appearing in (3.3.1) involving atoms in this unit cell are identified. This unit cell has been designated '0' and hence at least one of the cell indices in (3.2.4) must be 0. The matrices (3.2.4) involving bond stretching can be obtained by a straightforward differentiation of (A1.6):

$$\Phi_{\mu\nu}\begin{pmatrix} 0 & \ell \\ j & i \end{pmatrix} = -\frac{k_r}{r^2}\left[\left(r_i^{\ell} - r_j^{0}\right)_{\mu}\left(r_i^{\ell} - r_j^{0}\right)_{\nu}\right] \qquad \text{(A1.8)}$$

where ℓ may or may not be '0'.

The bond angle bending terms are three body interactions and evaluation of (3.2.4) for these terms is dependent on which two of the three atoms are considered. Three cases arise from the differentiation of (A1.7):

(i)

$$\Phi_{\mu\nu}\begin{pmatrix} 0 & \ell \\ j & i \end{pmatrix} = -\frac{k_\theta}{r^2}\Big\{\left[\left(r_i^{\ell} - r_j^{0}\right)_{\mu} + \left(r_k^{\ell'} - r_j^{0}\right)_{\mu}\right]\left(r_k^{\ell'} - r_j^{0}\right)_{\nu}$$

$$- \cos\theta\left[\left(r_i^{\ell} - r_j^{0}\right)_{\mu} + \left(r_k^{\ell'} - r_j^{0}\right)_{\mu}\right]\left[\left(r_i^{\ell} - r_j^{0}\right)_{\nu} + \left(r_k^{\ell'} - r_j^{0}\right)_{\nu}\right]$$

$$+ \cos^2\theta\left[\left(r_i^{\ell} - r_j^{0}\right)_{\mu} + \left(r_k^{\ell'} - r_j^{0}\right)_{\mu}\right]\left(r_i^{\ell} - r_j^{0}\right)_{\nu}\Big\} \qquad \text{(A1.9)}$$

(ii)

$$\Phi_{\mu\nu}\begin{pmatrix} 0 & \ell \\ i & j \end{pmatrix} = -\frac{k_\theta}{r^2}\Big\{\left(r_k^{\ell'} - r_j^{\ell}\right)_{\mu}\left[\left(r_i^{0} - r_j^{\ell}\right)_{\nu} + \left(r_k^{\ell'} - r_j^{\ell}\right)_{\nu}\right]$$

$$- \cos\theta\left[\left(r_i^{0} - r_j^{\ell}\right)_{\mu} + \left(r_k^{\ell'} - r_j^{\ell}\right)_{\mu}\right]\left[\left(r_i^{0} - r_j^{\ell}\right)_{\nu} + \left(r_k^{\ell'} - r_j^{\ell}\right)\right]$$

$$+ \cos^2\theta\left(r_i^{0} - r_j^{\ell}\right)_{\mu}\left[\left(r_i^{0} - r_j^{\ell}\right)_{\nu} + \left(r_k^{\ell'} - r_j^{\ell}\right)\right]\Big\} \qquad \text{(A1.10)}$$

(iii)

$$\Phi_{\mu\nu}\begin{pmatrix} o & \ell' \\ i & k \end{pmatrix} = + \frac{k_\theta}{r^2}\Big\{ (r_k^{\ell'} - r_j^{\ell})_\mu (r_i^o - r_j^{\ell})_\nu$$

$$- \cos\theta \left[(r_i^o - r_j^{\ell})_\mu (r_i^o - r_j^{\ell})_\nu + (r_k^{\ell'} - r_j^{\ell})_\mu (r_k^{\ell'} - r_j^{\ell})_\nu \right]$$

$$+ \cos^2\theta \, (r_i^o - r_j^{\ell})_\mu (r_k^{\ell'} - r_j^{\ell})_\nu \Big\} \qquad \text{(A1.11)}$$

Recall that the subscript j appearing in (A1.9)-(A1.11) designates a vertex atom and it should be noted that (A1.11) involves second nearest neighbours while (A1.9) and (A1.10) represent first nearest neighbour interactions.

Since one of the cell indices is always 0, the notation of (A1.8) - (A1.11) can be changed, rewriting these matrices as

$$\Phi_{\mu\nu}\begin{pmatrix} \ell \\ j \quad i \end{pmatrix} \qquad \text{(A1.12)}$$

if it is remembered that the left atom index represents an atom in cell 0. This form is now equivalent to that appearing in (3.2.8)

Lastly, there is one form of the matrix (3.2.4) which has not been considered, namely

$$\Phi\begin{pmatrix} o \\ i \quad i \end{pmatrix} \qquad \text{(A1.13)}$$

In principle this can be evaluated using the same procedure used in arriving at (A1.8) - (A1.11). However it proves to be more expedient to use the condition (Maradudin et al., 1963)

$$\sum_{\ell,j} \Phi_{\mu\nu}\binom{\ell}{i\,j} = 0 \qquad \text{(A1.14)}$$

from which it follows that

$$\Phi\binom{0}{i\,i} = -\sum_{\ell\neq 0} \Phi_{\mu\nu}\binom{\ell}{i\,i} - \sum_{\ell}\sum_{j\neq i} \Phi_{\mu\nu}\binom{\ell}{i\,j} \qquad \text{(A1.15)}$$

For the 2H compounds there are 156 matrices obtained from (A1.8) - (A1.11) and another six obtained from (A1.15) which must considered. These are summed according to (3.2.8) and result in the 18x18 dynamical matrix appearing in (3.2.9). The explicit form of the dynamical matrix, for the special case of $\vec{q} = 0$, is presented below. (For the more general case of $\vec{q} \neq 0$ there are many additional non-zero terms). The labelling of the atoms, ie. i and j (or alternatively K and K′ as in (3.2.9)), is as indicated in Fig. 2.1b.

i / j	1			2			3			4			5			6		
1	c5	0	0				c1	0	0	c1	0	0						
	0	c5	0				0	c1	0	0	c1	0						
	0	0	c6				0	0	c2	0	0	c2						
2				c5	0	0							c1	0	0	c1	0	0
				0	c5	0							0	c1	0	0	c1	0
				0	0	c6							0	0	c2	0	0	c2
3	c1	0	0				c7	0	0	c9	0	0				c3	0	0
	0	c1	0				0	c7	0	0	c9	0				0	c3	0
	0	0	c2				0	0	c8	0	0	c10				0	0	c4
4	c1	0	0				c9	0	0	c7	0	0	c3	0	0			
	0	c1	0				0	c9	0	0	c7	0	0	c3	0			
	0	0	c2				0	0	c10	0	0	c8	0	0	c4			
5				c1	0	0				c3	0	0	c7	0	0	c9	0	0
				0	c1	0				0	c3	0	0	c7	0	0	c9	0
				0	0	c2				0	0	c4	0	0	c8	0	0	c10
6				c1	0	0	c3	0	0				c9	0	0	c7	0	0
				0	c1	0	0	c3	0				0	c9	0	0	c7	0
				0	0	c2	0	0	c4				0	0	c10	0	0	c8

where the terms appearing in the dynamical are given by

$$C1 = -\frac{1}{2}\frac{1}{\sqrt{m_x m_M}}\left(\frac{a}{r}\right)^2\left[k_r + 2(1-\cos\psi)^2 k_\psi + 2(1-\cos\theta)^2 k_\theta + 2(1-\cos\phi)^2 k_\phi\right]$$

$$C2 = \frac{-3}{\sqrt{m_x m_M}}\left(\frac{z}{r}\right)^2\left[k_r + 4(1-\cos\theta)^2 k_\theta + 4(1-\cos\phi)^2 k_\phi\right]$$

$$C3 = -\frac{a^2}{m_x}\left[\frac{1}{2}\frac{1}{R1^2}k_{R1} + 2\frac{1}{R2^2}k_{R2}\right]$$

$$C4 = -\frac{12}{m_x}w^2\left[\frac{1}{R1^2}k_{R1} + \frac{1}{R2^2}k_{R2}\right]$$

$$C5 = -2\sqrt{\frac{m_x}{m_M}}\,C1$$

$$C6 = -2\sqrt{\frac{m_x}{m_M}}\,C2$$

$$C7 = -\left(\sqrt{\frac{m_M}{m_x}}\,C1 + C3 + C9\right)$$

$$C8 = -\left(\sqrt{\frac{m_M}{m_x}}\,C2 + C4 + C10\right)$$

$$C9 = +\frac{1}{2}\frac{1}{m_x}\left(\frac{a}{r}\right)^2(1-\cos\psi)^2 k_\psi$$

$$C10 = -\frac{3}{m_x}\left(\frac{z}{r}\right)^2(1+\cos\psi)^2 k_\psi$$

Appendix II - Dispersion Curves for Tantalum and Niobium Disulphide

Feldman's VFF model #2 (Feldman, 1982) included a phenomenological q-dependent term, D'(q), which was added to the dynamical matrix to fit the observed flattening of the Σ_1 acoustic branch in $TaSe_2$. The same term predicted the Kohn anomaly observed in $NbSe_2$ remarkably well.

The effect of D'(q) on the dispersion curves of TaS_2 along Σ is shown in Fig. A2.1. The term has a small effect on the higher freqency optic modes and inclusion of the term does not affect the discussion of section 6.2.

Since D'(q) was fit to data for $TaSe_2$ and since the Σ_1 acoustic branch is very sensitive to k_θ , which is undetermined for TaS_2, Fig. A2.1 gives only a qualitative picture of the expected dispersion curves in TaS_2. However it remains of interest to see how closely Fig. A2.1 predicts the actual curves for TaS_2 should they become available from neutron data.

For completeness, the dispersion curves for 2H-NbS_2 based on the force constants of Table 5.2 are presented in Fig. A2.2. Since the Raman spectrum of NbS_2 does not show a prominent second order feature the existence of a Kohn anomaly is somewhat more questionable than in TaS_2 and hence the D'(q) term has not been included in the dispersion curves of Fig. A2.2.

The speed of sound predicted by the model and based on the initial slope of the LA dispersion curve in Fig. A2.2 is 5.6×10^5 cm/sec.

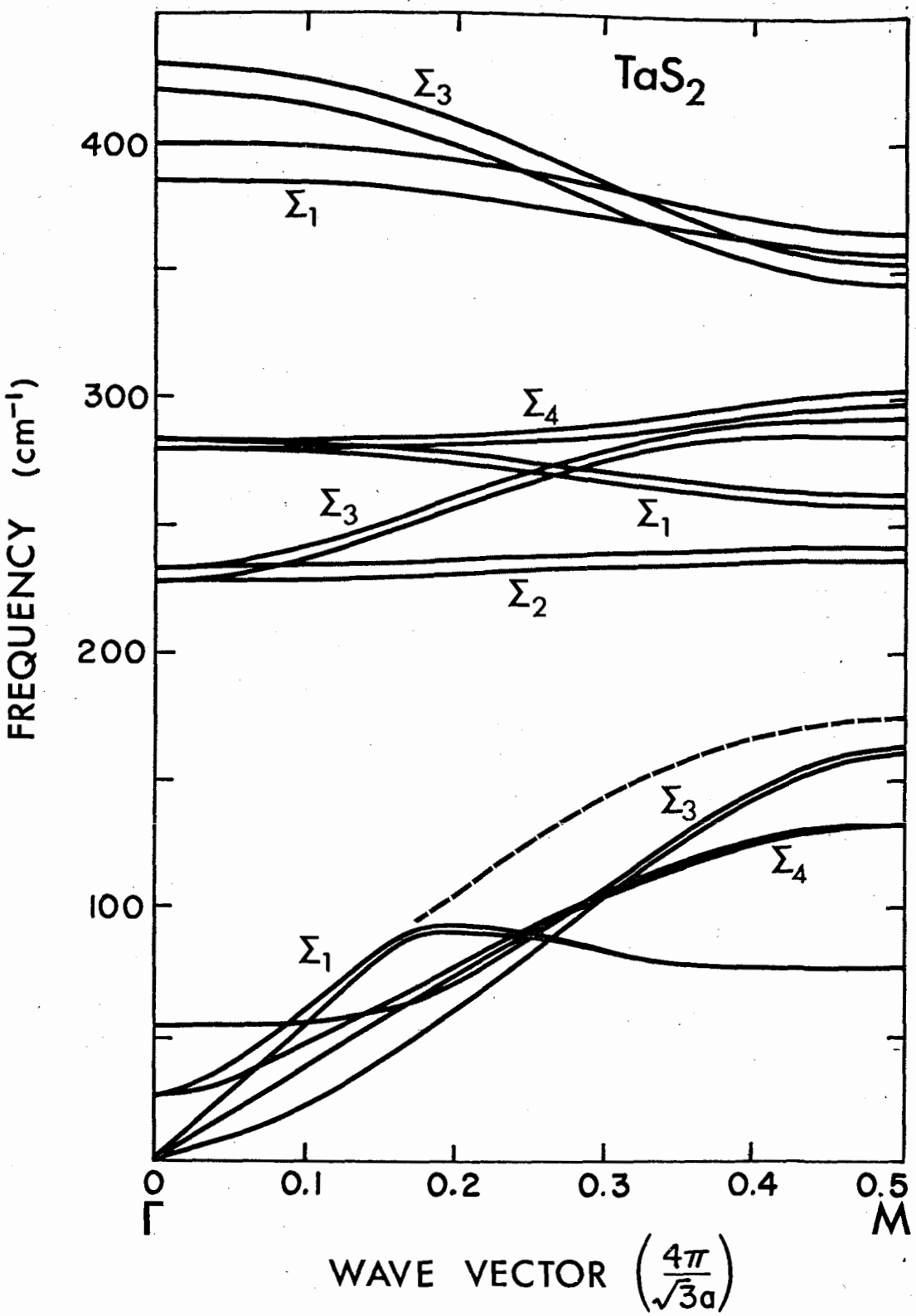

Figure A2.1 - Phonon dispersion curves for 2H-TaS_2 along ΓM when Feldman's D'(q) term has been included in dynamical matrix. Dashed line corresponds to dispersion curves without D'(q) term.

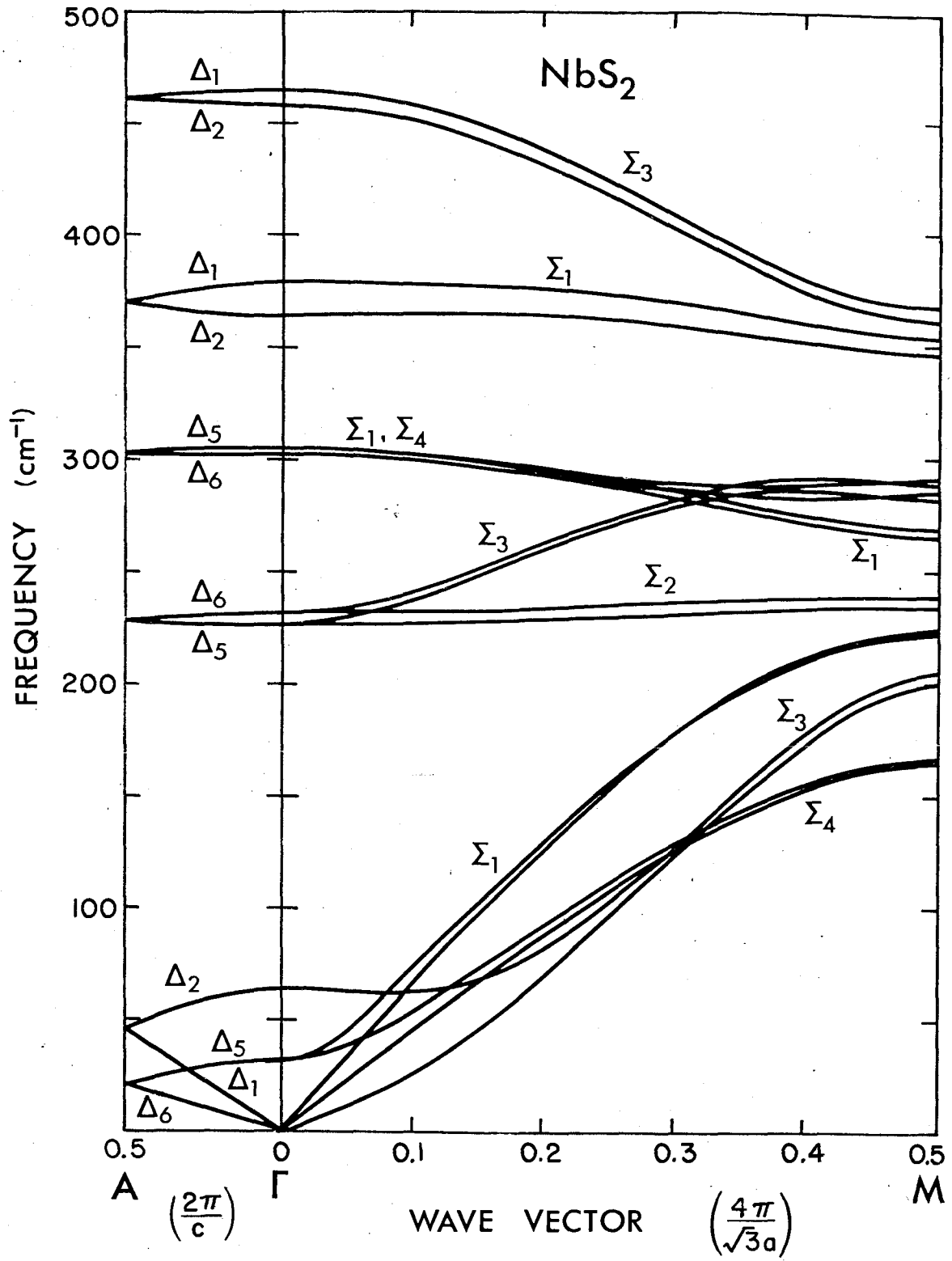

Figure A2.2 - Phonon dispersion curves for 2H-NbS_2 along ΓM and ΓK (based on VFF model).

References

O. P. Agnihorti, H. K. Sehgal and A. K. Garg, Sol. St. Comm. 12, 135 (1973)

N. W. Ashcroft and N. D. Mermin, Solid State Physics, Holt, Rinehart and Winston, Philadelphia (1976)

M. Born and K. Huang, Dynamical Theory of Crystal Lattices, Oxford University Press, London (1954)

R. A. Bromley, Phil. Mag. 23, 1417 (1971)

G. Burns, Introduction to Group Theory with Applications, Academic Press, New York (1977)

E. Burstein, Phonons and Phonon Interactions, ed. by T. A. Bak, p.276, W. A. Benjamin, New York (1964)

J. R. Duffey, R. D. Kirby and R. V. Coleman, Proc. Int. Conf. on Light Scattering in Solids, ed. by M. Balkanski, R. C. C. Leite and S. P. S. Porto, p.383, Flammarion, Paris (1976)

W. G. Fateley, F. R. Dollish, N. T. McDevitt and F. R. Bentley, Infrared and Raman Selection Rules for Molecular and Lattice Vibrations: The Correlation Method, John Wiley and Sons, New York (1972)

J. L. Feldman, Phys. Rev. B 25, 7132 (1982)

W. G. Fisher and M. J. Sienko, Inorg. Chem. 19, 39 (1980)

V. Heine, Group Theory in Quantum Mechanics, Pergamon Press, London (1960)

J. A. Holy, M. V. Klein, W. L. McMillan and S. F. Meyer, Phys. Rev. Lett. 37, 1145 (1976)

J. A. Holy, Ph.D Thesis, University of Illinois at Urbana-Champaign (1977)

M. H. Jericho, A. M. Simpson and R. F. Frindt, Phys. Rev. B 22, 4907 (1980)

D. R. Karecki, Ph.D Thesis, Simon Fraser University, Burnaby, B.C. (1980)

M. V. Klein, Phys. Rev. B 25, 7192 (1982)

R. Leonelli, M. Plischke and J. C. Irwin, Phys. Rev. Lett. 45, 1291 (1980)

R. A. Loudon, Proc. Roy. Soc. A 275, 218 (1963)

R. A. Loudon, Adv. Phys. 13, 423 (1964)

R. A. Loudon, The Quantum Theory of Light, Oxford University Press, London (1973)

G. Lucovsky, Proc. Int. Conf. on Atomic Spectroscopy, p.429, Prague (1977)

P. F. Maldague and J. C. Tsang, Proc. Int. Conf. on Lattice Dynamics, ed. by M. Balkanski, p. 602, Flammarion, Paris (1977)

A. A. Maradudin, E. W. Montroll and G. H. Weiss, Theory of Lattice Dynamics in the Harmonic Approximation, Academic Press, New York (1963)

D. E. Moncton, J. D. Axe and F. J. DiSalvo, Phys. Rev. Lett. 34, 734 (1975)

D. E. Moncton, J. D. Axe and F. J. DiSalvo, Phys. Rev. B 16, 801 (1977)

S. Nakashima, Y. Tokuda, A. Mitsuishi, R. Aoki and Y. Hamaue, Sol. St. Comm. 42, 601 (1982)

R. J. Nemanich and S. A. Solin, Phys. Rev. B 20, 392 (1979)

S. Onari, T. Arai, R. Aoki and S. Nakamura, Sol. St. Comm. 31, 577 (1979)

M. Plischke, K. K. Bardhan, R. Leonelli and J. C. Irwin, to be published in Can. J. Phys.

D. R. Powell and R. A. Jacobson, J. Solid St. Chem. 37, 140 (1981)

M. Schluter, Electrons and Phonons in Layered Crystal Structures, ed. by T. J. Wieting and M. Schluter, p.1, D. Reidel, Dordrecht, Holland (1979)

G. A. Scholz and R. F. Frindt, Mat. Res. Bull. 15, 1703 (1980)

G. A. Scholz, R. F. Frindt and A. E. Curzon, Phys. Stat. Sol. A 71, 531 (1982a)

G. A. Scholz, R. F. Frindt and A. E. Curzon, Phys. Stat. Sol. A 72, 375 (1982b)

M. S. Skolnick, S. Roth and H. Alms, J. Phys. C 10, 2523 (1977)

J. C. Slater, Symmetry and Energy Bands in Crystals, Dover Publications, New York (1965)

R. Sooryakumar, M. V. Klein and R. F. Frindt, Phys. Rev. B 23, 3222 (1981)

S. Sugai, K. Murase, S. Uchida and S. Tanaka, Sol. St. Comm. 40, 399 (1981)

M. Tinkham, Group Theory and Quantum Mechanics, McGraw-Hill, New York (1964)

J. C. Tsang, J. E. Smith and M. W. Shafer, Phys. Rev. Lett. 37, 1407 (1976)

J. C. Tsang, J. E. Smith and M. W. Shafer, Sol. St. Comm. 27, 145 (1978)

J. L. Verble and T. J. Wieting, Phys. Rev. Lett. 25, 362 (1970)

J. L. Verble, T. J. Wieting and P. R. Reed, Sol. St. Comm. 11, 941 (1972)

N. Wada, M. V. Klein and H. Zabel, Proc. Int. Conf. on Physics of Intercalation Compounds, ed. by L. Pietronero and E. Tosatti, Springer-Verlag, Berlin (1981)

N. Wakabayashi, H. G. Smith and R. Shanks, Phys. Letters 50A, 367 (1974)

N. Wakabayashi, H. G. Smith and R. M. Nicklow, Phys. Rev. B 12, 659 (1975)

C. S. Wang and J. M. Chen, Sol. St. Comm. 14, 1145 (1974)

M. S. Whittingham, Prog. Solid St. Chem 12, 41 (1978)

T. J. Wieting, Sol. St. Comm. 12, 931 (1973)

J. A. Wilson and A. D. Yoffe, Adv. Phys. 18, 193 (1969)

J. A. Wilson, F. J. DiSalvo and S. Mahajan, Adv. Phys. 24, 117 (1975)